Nanoscale

Effects of Morphology and Temperature on the Tensile Characteristics of Carbon Nitride Nanothreads

Journal:	*Nanoscale*
Manuscript ID	NR-ART-04-2020-003206
Article Type:	Paper
Date Submitted by the Author:	23-Apr-2020

Complete List of Authors:	Fu, Yuequn; Norwegian University of Science and Technology, Department of Structural Engineering Xu, Ke; Xiamen University Wu, Jianyang; Xiamen University, Department of physics; NTNU Fakultet for ingeniorvitenskap og teknologi Trondheim, Department of Structural Engineering Zhang, Zhiliang; Norwegian University of Science and Technology, Department of Structural Engineering He, Jianying; Norwegian University of Science and Technology, Department of Structural Engineering; NTNU,

Note: The following files were submitted by the author for peer review, but cannot be converted to PDF. You must view these files (e.g. movies) online.

Polytwistane_153.cif
Tube (3,0)_123456.cif
Tube (3,0)_1245.cif
IV-7.cif
Polymer I_3-3_25.cif
Polymer I_4-2_36.cif
Zipper polymer_24.cif

Effects of Morphology and Temperature on the Tensile Characteristics of Carbon Nitride Nanothreads

Yuequn Fu,[a] Ke Xu,[b] Jianyang Wu,[*a,b] Zhiliang Zhang[a] and Jianying He[*a]

[a]NTNU Nanomechanical Lab, Norwegian University of Science and Technology (NTNU), Trondheim 7491, Norway

[b]Department of Physics, Research Institute for Biomimetics and Soft Matter, Jiujiang Research Institute and Fujian Provincial Key Laboratory for Soft Functional Materials Research, Xiamen University, Xiamen 361005, PR China

Abstract: Very recently synthesized carbon nitride nanothreads (CNNTs) by compressing crystalline pyridine show outperformance in chemical and physical properties over diamond nanothreads. Here, using first-principle based ReaxFF molecular dynamics (MD) simulations, a comprehensive investigation on mechanical characteristics of seven experimentally synthesized CNNTs is performed. All the CNNTs exhibit unique tensile properties that change with molecular morphology, atomic arrangement and the distribution of nitrogen in the skeleton. CNNTs with more effective loading covalent bonds at cross-sections are more mechanically robust. Surprisingly, tiny CNNT with periodic unit structures of $5^4 6^2$-cage shows extreme ductility because of formation of linear polymer via 4-step dissociation-and-reformation of bonds at extremely low temperature of 1 to 15 K, however, it yields by brittle failure at one cross-section with low ductility at higher temperature, similar to other CNNTs at different temperatures, which offers a feasible way to design a kind of lightweight material that can be used in ultra-low temperature conditions, for example, harsh deep space environment. Results also show that temperature significantly affects the fracture stress and rupture strain but not the effective stiffness. Analysis of atomic bond orders and bond lengthening reveals that the unique nonlinear elasticity of CNNTs is attributed to the occurrence of local bond transformations. This study provides physical insights into the tensile characteristics of CNNTs for design and application of the CNNT-based nanostructures as multifunctional materials.

1 Introduction

As a unique element, carbon is able to form a variety of covalent bonds (s*p*, sp^2, and sp^3 hybridized)[1-3], resulting in various kinds of carbon-based nanostructures in natural and lab-settings. Recently, a new class of one-dimensional (1D) carbon nanostructures termed as diamond nanothreads (DNTs)[4-6] was synthesized by solid-state high-compression of crystalline hexagonal benzene. DNTs are structurally characterized by a core of long, ultrathin strand of sp^3-hybridized carbon atoms packed in a diamond-like tetrahedral motif[7]. Such 1D nanomaterials have attracted great attention in the past few years due to their unique physical[8-10] and chemical properties[11-13].

Mechanically, as a result of the diamond-like molecular core structure, DNTs are expected to exhibit excellent mechanical performances. To the best of our knowledge, there is no available experimental measurement of mechanical properties of tiny DNTs. Alternatively, a number of theoretical studies emerged for characterizing the mechanical properties of DNTs.[8, 14-21] Based on those pioneering investigations, It can be summarized that tiny DNTs are mechanically robust and its mechanical properties are strongly dependent on numerical methods, the internal atomic structures such as defects, molecular morphology, dehydrogenation, functional groups on surface and so on, as well as external temperature.[8, 20-23] By using ReaxFF-based molecular dynamic (MD) simulations, it was explored that the axial stiffness of DNTs ranges from approximately 665 - 850 GPa, depending on the density of Stone-Wales (SW) defects[20]. By AIREBO-based MD simulations, it was found that the axial stiffness of DNTs varies from around 700-950 GPa and the sp^3-bonded DNT shows a transition from brittle to ductile behavior by increasing the number of SW defects[8]. The molecular morphology of DNTs plays an important role in the tensile properties [21, 22]. Using ReaxFF-based MD simulations, the DNTs with linear atomic configuration has higher tensile stiffness of 360 - 730 GPa, while the other with helical morphologies exhibit lower tensile stiffness in the range of 75-375 GPa[21]. Interestingly, dehydrogenation of DNTs is able to reinforce the stiffness, rigidity, and ductility with around 1-fold, 2-folds and 3-folds as much as their original counterparts, respectively, yet negligibly influences on their own primeval configurations and

stabilization[21]. Notably, the dehydrogenated DNTs composed of purely hexagonal carbon rings exhibit superior mechanical properties to other DNTs[21]. By using density functional theory calculations (DFT), it was shown that introduction of various functional groups (-CH_3, -NH_2, -OH, -F) on the surface of DNTs plays a negligible role on their mechanical properties[23]. Moreover, it is observed that both tensile strength and failure strain are reduced with increasing temperature, yet not for the tensile stiffness and elastic nonlinearities[11, 20, 21].

Because of their outstanding mechanical properties, DNTs show versatile applications in many fields[24-26]. For instance, because of the strong mechanical interlocking effect at the interface between DNTs, pull-out tests showed the DNT bundle possesses an interface transfer load of over 2-folds that of the carbon nanotube (CNT) bundle, indicating that DNT is a promising candidate for fabricating next-generation carbon fibers [7]. Similarly, the DNTs can be considered as a new filler for nanocomposites because the noncovalent interfacial load transfer is greatly enhanced by SW defects induced irregular surfaces[27]. Similar to the case of diamond nanowires, DNTs can be also applied to the AFM tips to enhance the resolution because it is sharp enough[9].

More recently, similar carbon-based nanostructures called carbon nitride nanothreads (CNNTs) were creatively synthesized by compressing crystalline pyridine[28]. The introduction of nitrogen in this new nanothread is expected to play better in processability and altering photoluminescence[28]. Moreover, it was expected that CNNTs show reduction in the bandgap and can be utilized for important bio-imaging applications[28]. To date, however, there is only one available study characterizing the elastic properties of CNNTs by DFT calculations[29]. It was revealed that fully-saturated CNNTs possess superior stiffness and strength to partially-saturated ones. Nevertheless, the mechanical behaviors of tiny CNNTs still remain largely unknown yet, particularly for the plasticity, the effects of temperature and dynamical information of the local bond-order (BO) of carbon and nitrogen and the bond-lengthening under axial straining, which limits their applications as a building block in finite-temperature environment. In this work, a series of Reaxff-based MD simulations are performed to systematically investigate the mechanical characteristics

of seven experimentally synthesized CNNTs with identical chemical formula of $((CH_5)N)_n$ but with different morphologies at temperatures varying from 1-1500 K. It is revealed that, the tensile characteristics of CNNTs vary vastly with molecular morphology, although they possess identical chemical compositions. Also, the temperature plays a crucial role on their mechanical performances. Intriguingly, Polymer I_3-3_25 shows a mechanical transition from brittle behavior to extraordinarily ductile behavior at a critical temperature of 15 K. Below 15 K, it is able to yield superior tensile ductility (> 190%), originating from its 4-step dissociation-vs-reformation of periodic unit structures of $5^4 6^2$-cage, while above 15 K, it exhibits very limited elongation (< 25%) due to catastrophic fracture at one tiny cross-section, similar to other CNNTs. Such high strength and extreme deformability of Polymer I_3-3_25 is particularly encouraging, making it a lightweight material that can be used as robust energy-absorbed fibers under outer-space and extreme experimental environments.

2 Atomic Models and Methodology

To date, more than 50 enumerated DNTs with the chemical formula $((CH)_6)$ have been proposed, and some of them have been experimentally synthesized in lab-settings[4, 30, 31]. As a consequence of unique properties of DNTs, there are attempts to derivatize the DNTs. Very recently, CNNTs have been proposed and also synthesized[28, 32, 33]. Here, in order to systematically understand the tensile mechanical characteristics of CNNTs, seven different CNNTs with chemical formula $((CH_5)N)_n$ synthesized by Chen et al.[28] were taken into investigation. All those CNNTs consist of various polygons such as pentagon, hexagon, heptagon, and octagon. To distinguish from each other, as suggested by Chen et al.[28], the seven different CNNTs were named as Tube (3,0)_123456, Tube (3,0)_1245, Polymer I_3-3_25, Polymer I_4-2_36, Polytwistane_153, Zipper polymer_24, and IV-7, respectively. The way of the nomenclature for substituted nanothreads has been explored with the chemical formula $((CH)_5X)_n$, where X is heteroatom or -CR substituent.[34] In this study, for the case of CNNTs with chemical formula of $((CH)_5N)_m$, the naming convention of the enumerated DNTs is applied, which includes an integer string that tells where the nitrogen atoms are in the six-element ring. For instance, the doped nitrogen atoms in Tube (3,0)_123456

replace the C-H pairs whose positions are in 1, 2, 3, 4, 5, and 6 of six sequential rings in a single DNT.[28] Figure 1 shows both side- and top-views of molecular configurations of those CNNTs. Apparently, all CNNTs are linearly molecular configurations. The blue sphere indicates the locations of nitrogen in the CNNTs. To avoid the effects of end boundaries on the mechanical properties, a periodic boundary condition (PBC) was imposed along the axial direction of the CNNTs. To exclude the repeated calculation of non-bonded van der Waals (vdW) interactions in the CNNTs, the axial lengths of all CNNTs were constructed to be approximately 30 Å. To evaluate the density of strain energy and loading stress, the diameter of all CNNTs was kept as 0.5 nm[20], which is identical to that of straight DNTs.

All the classic MD simulations were performed by using the Large-scale Atomic-Molecular Massively Parallel Simulator (LAMMPS) code package. The first-principles-based ReaxFF potential was utilized to describe the atomic interactions in the CNNTs nanotructures[35]. The ReaxFF potential is capable of capturing all the possible interactions such as covalent bonds, coulombic interactions, dispersion and other non-bonded interacting forces[35]. Furthermore, based on values of bond order, chemical reactions such as formation and dissociation of chemical bonds can be also mimicked by this forcefield. It was shown that the ReaxFF potential well predicts the structural and mechanical properties of various carbon-dominated nanostructures such as CNTs, carbon nitride sheets, diamond, and other various nanostructures[36-39]. In the present study, the version of ReaxFF potential parameterized by Budzien et al. [40]was utilized.

Before MD relaxations, standalone CNNTs were quasi-statically relaxed to a local minimum energy configuration with an energy tolerance and a force tolerance of 1.0×10^{-4} Kcal/mole and 1.0×10^{-4} Kcal/mole·Å, respectively. Subsequently, free-standing CNNTs were completely relaxed with a long 200,000 timesteps at zero pressure along the axial direction. The NPT ensemble (constant number of particles, constant pressure, and constant temperature) was used in this MD relaxation. To maintain the assigned temperature and pressure, the Nosé-Hoover thermostat and Nosé-Hoover barostat methods with

damping timesteps of 100 and 1000 were utilized. By integrating Newton's motion of atoms in the CNNTs, a small timestep of 0.1 fs was used with the velocity-Verlet algorithm.

To examine the tensile characteristics of the CNNTs, the mechanical loads along the axial direction were applied by the deformation technique under NVT (constant number of particles, constant volume, and constant temperature) ensemble. A reasonable straining rate of 1.0×10^8 s^{-1} was applied in the elongation MD calculations. The increment of elongation was imposed on the CNNTs every 1000 timesteps. Atomic stress in the CNNTs is computed based on the virial definition of stress. Global tensile stress is realized by summing the stress of all atoms in the CNNT structures. The tensile Young's modulus (E) was obtained by the slope of linearly fitting the initial stress-strain curves.

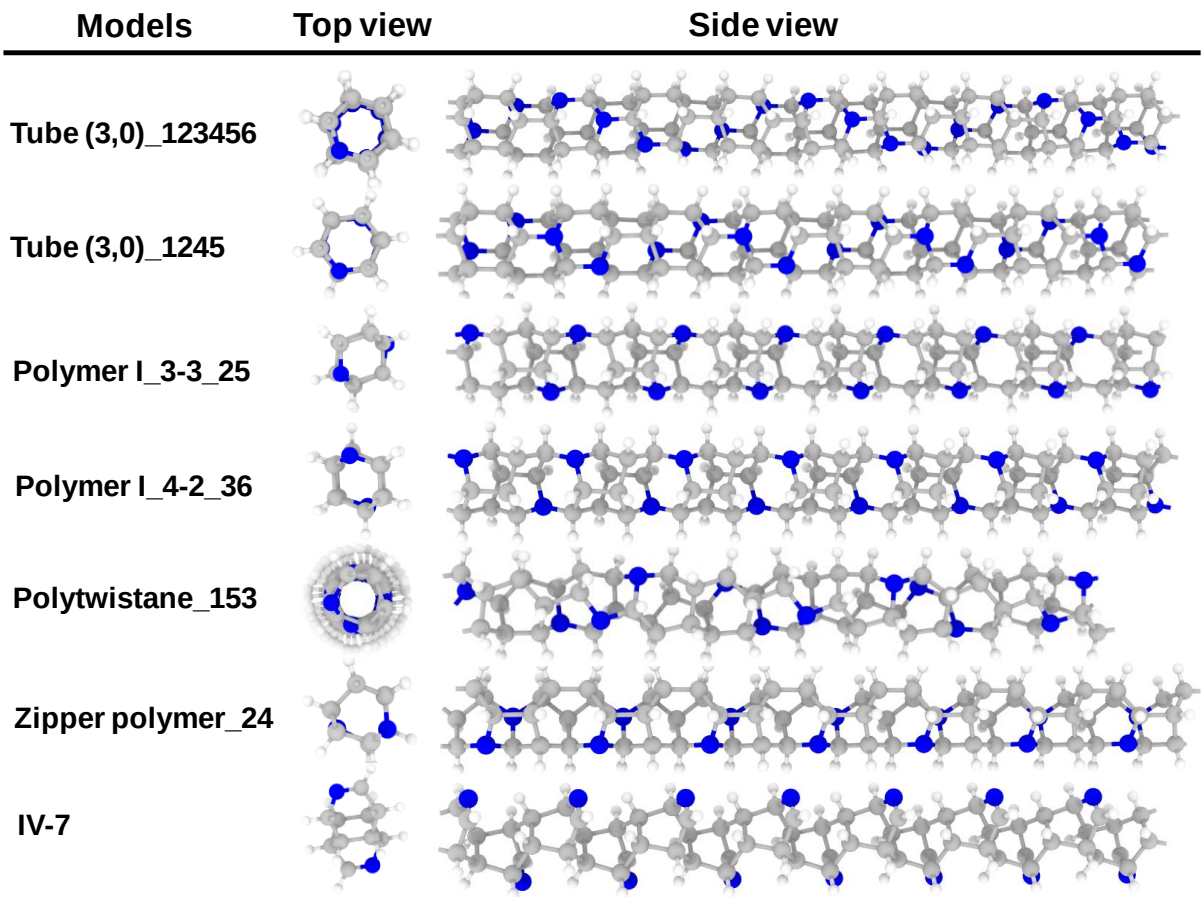

Figure 1 Molecular configurations of seven distinct CNNTs including Tube (3,0)_123456, Tube (3,0)_1245, Polymer I_3-3_25, Polymer I_4-2_36, Polytwistane_153, Zipper polymer_24, and IV-7. Left and right show the top-viewed and side-viewed snapshots.

3 Results and Discussion

3.1 Role of Morphology on the Tensile Characteristics of CNNTs

3.1.1 Tensile Properties of CNNTs

Initially, the effects of morphology on the tensile properties of CNNTs are examined at extremely low temperature 1 K. The setup of low temperature is purposed for eliminating the effect of thermal kinetic. Figure 2a compares the axial tensile stress-strain responses of all seven stable CNNTs at 1 K. Obviously, all investigated CNNTs exhibit strong nonlinearity in the tensile stress-strain curves, and the feature of nonlinearity of mechanical responses is molecular morphology dependent. However, all CNNTs present three stages of elastic responses. The initial elastic deformations are characterized by reduction in tensile stiffness with increasing strain. Interestingly, the second elastic responses are mainly characterized by the drop of tensile stress in the curves. Such irregular changes in loading stress are mainly associated with the occurrence of sudden C-C bond and C-C-C angular transformations during the intermediate elongation[41, 42]. It is noted that those bonds and angular transformations are recoverable when the load is removed. In the last elastic deformation response, increases in the loading stresses with increasing strain are observed. By excluding the Polymer I_3-3_25 CNNT, other CNNTs are yielded by brittle rupture under overloading, as indicated by sudden drops of loading stresses to zero in the curves. Remarkably, the Polymer I_3-3_25 CNNT fails in a ductile fracture mode, as indicated by a uniquely sawtooth characteristic in the loading curves after the elastic response. Such sawtooth-shaped tensile response has been also observed in helically coiled CNTs.[43] Similar to the case of helically coiled CNTs, an uniform distribution of dissociation and reformation of bonds along the backbone of the nanothread is responsible for its extraordinary tensile response. Detail information is discussed in the following section.

Figure 2b shows the resulting axial tensile Young's moduli of all studied CNNTs. It is shown that, depending on the molecular structures, CNNTs exhibit high tensile stiffness varying from around 300 - 920 GPa, respectively, which are comparable to that of CNTs[8, 20-23]. In terms of tensile stiffness, they are sorted from the highest to the lowest values as: Tube (3,0)_1245 > Zipper polymer_24 > Tube

(3,0)_123456 > Polytwistane_153 > Polymer I_3-3_25 > Polymer I_4-2_36 > IV-7. Those distinct tensile stiffnesses can be informed from their uniquely localized atomic arrangements. The low tensile stiffnesses of IV-7, Polymer I_4-2_36, and Polymer I_3-3_25 are mainly attributed to their weak cross-sections composed of two effective covalent bonds. The lowest tensile stiffness of IV-7 is because two effective C-C covalent bonds are uniformly distributed in the cross-section and the loading skeleton is armchair-like motif from one side-view. The higher tensile stiffnesses of Polymer I_4-2_36 and Polymer I_3-3_25 mainly come from the stiffer zigzag-like motifs of the loading skeleton. Notably, the small difference of tensile stiffnesses of similar morphological Polymer I_4-2_36 and Polymer I_3-3_25 is due to their different effective bonds and bond angles in the loading skeleton. In comparison, as a result of three effective covalent bonds in their loading cross-sections, Tube (3,0)_1245, Tube (3,0)_123456, Zipper polymer_24 and Polytwistane_153 exhibit high tensile stiffness. Similarly, their different tensile stiffnesses are primarily from the distinct atomic arrangements or locations of nitrogen (N) doping in the skeleton. Analogous to the DNTs[21, 43], Tube (3,0) CNNTs show outperformance of mechanical stiffness as a result of their diamond-like atomic structures. It is noted that free-standing Zipper polymer_24 is intrinsically circular-shaped morphology (Figure S1), resulting in that straight Zipper polymer_24 is the second stiffest CNNT due to pre-strained carbon bonds, angles, and torsions in the skeleton. Polytwistane_153 composed of hexagonal ring is the fourth stiffest CNNT due to its small bond angles that are easier to stretch. Intriguingly, comparing to the case of Polymer I_4-2_36 and Polymer I_3-3_25, similar morphological but different N-doped Tube (3,0)_1245 and Tube (3,0)_123456 CNNTs yield different tensile stiffnesses. Tube (3,0)_1245 with non-uniform N-doping exhibits higher tensile stiffness over Tube (3,0) composed of only carbon atoms in the skeleton, whereas Tube (3,0)_123456 with uniform N-doping is mechanically softer than non-doped Tube (3,0).

Figure 2c shows the resulting axial yield strength of all studied CNNTs. Depending on the molecular structures, investigated CNNTs exhibit high tensile yield strengths varying from around 45 -120 GPa, which are also of the same order of magnitude as that of CNTs[21]. In terms of yield strength, they are ranked

as: Tube (3,0)_1245 > Tube (3,0)_123456 > Polytwistane_153 > Polymer I_4-2_36 > Zipper polymer_24 > Polymer I_3-3_25 > IV-7. By comparison, there are slightly differences in the rank between tensile stiffness and yield strength, however, it can be roughly summarized that CNNTs with more effective bonds in the cross-section are mechanically stiffer and stronger. As is seen, CNNTs with energy-favorable hexagons and three effective bonds in the cross-section are mechanically stronger. Among them, Tube (3,0)_1245 is also the strongest CNNT. However, IV-7 with non-energy-favorable non-hexagons and two effective bonds in the cross-section is the weakest CNNT. It is noticed that differing from the tensile stiffness, Zipper polymer_24 shows the third-lowest yield strength because the load stress is mainly concentrated on the pre-strained carbon chain in the skeleton. With regard to the Polymer I CNNTs, their yield strengths are inversely ranked compared to the rank of tensile stiffness, suggesting the trade-off of mechanical stiffness and strength in specific DNTs by chemical doping[44]. The MD results reported here suggest that CNNTs show desirable mechanical properties and are mechanically competitive with CNTs, while Polymer I_3-3_25 is outperforming CNTs in axial deformability at extremely low temperature.

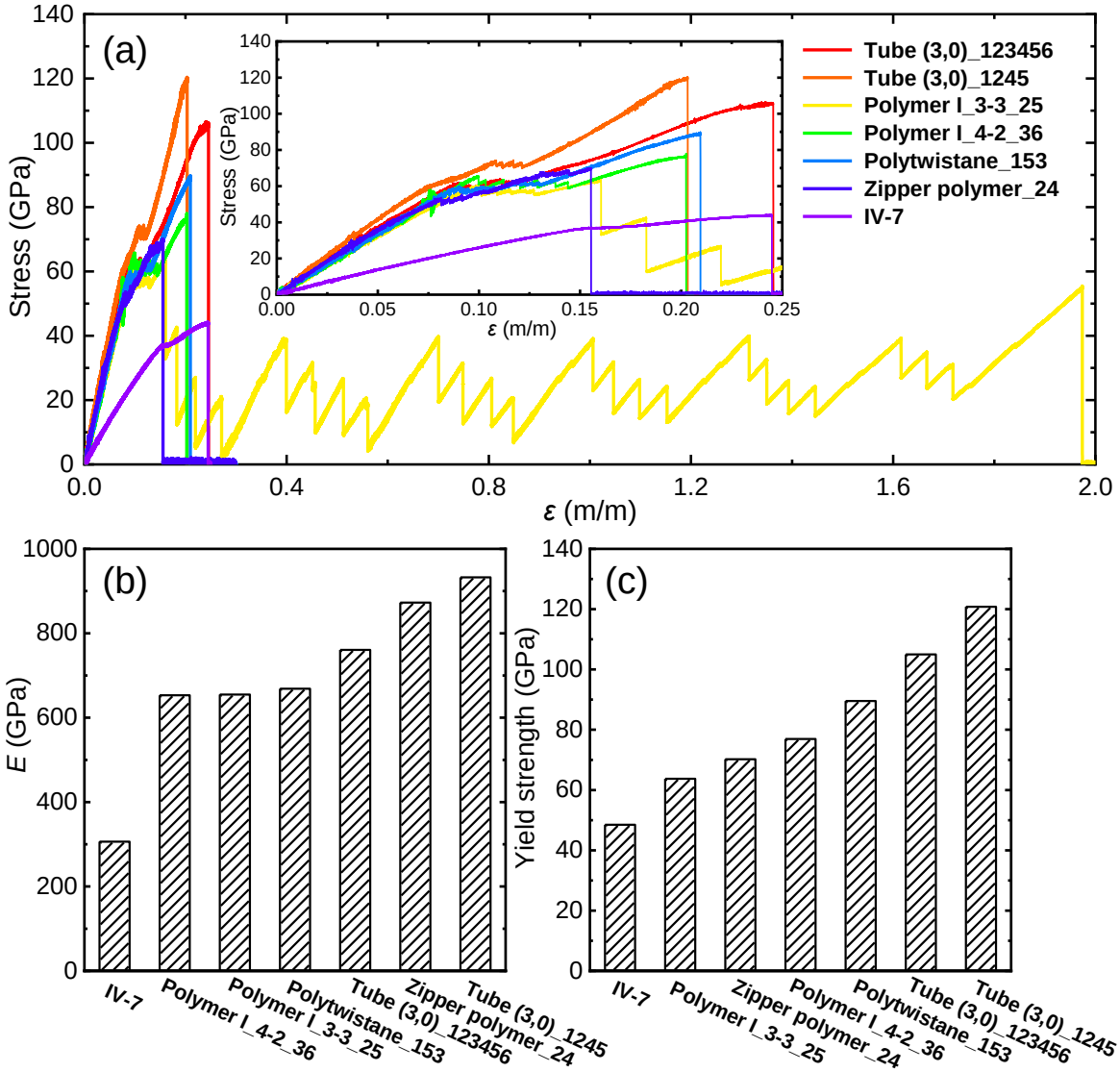

Figure 2 Tension of 7 different CNNTs at low temperature 1 K. (a) Tensile stress-strain responses of Tube (3,0)_123456, Tube (3,0)_1245, Polymer I_3-3_25, Polymer I_4-2_36, Polytwistane_153, Zipper polymer_24, and IV-7 CNNTs, (b) and Young's moduli (*E*) and (c) yield strength of those 7 CNNTs.

3.1.2 Dynamics of Atomic BOs in CNNTs during Elongation

In order to examine the chemical bond information of the mechanical deformation, the variation in the atomic BOs with axial elongation for all investigated CNNTs is studied. Figure 3 shows the total BOs of one carbon atom situated at the breaking sites as a function of tension strain for all studied CNNTs, as well as typical motifs of the carbon with neighboring atoms that are red- and green-highlighted. Prior to elongation (zero strain), the selected carbon atoms of all CNNTs show total BOs of about 3.9[21]. This

explains that their chemical bonding configurations are sp^3-bond, differing from the sp^2-bonding in both graphene and CNTs[45]. As seen from Figure 3, all the CNNTs show strong nonlinearity in the total BOs - strain curves of the selected carbon atoms. However, the selected carbon atoms undergo different evolutions of total BOs under axial tension, indicating their different localized deformation including the bond, angular and torsional deformations. Prior to failure, IV-7 shows smooth reduction in the BO with increasing strain. However, there are multiple singularities identified in the total BOs – strain curves for other CNNTs. As the elongation reaches critical strains, it is observed sudden rise in the total BOs of carbon for other CNNTs. This indicates structural transformation of bond, angular and torsional configurations, resulting in the corresponding sudden changes in the loading stresses of Figure 2a. Notably, Zipper polymer_24 shows two deep drops of total BOs of the carbon. As the elongation is over the failure strains, the total BOs of the selected carbon atom dramatically reduces. This results from the separation of the neighboring atoms, as seen from the insets. Particularly, the selected carbon atom of Polymer I_3-3_25 shows sawtooth-like characteristics in the total BOs-strain curves, corresponding to the unique sawtooth-shaped tensile stress-strain curves in Figure 2a.

Figure 4 plots the variation in the total BOs of one nitrogen atom in the vicinity of the breaking zone with axial tension strain for all investigated CNNTs. The highlighted insets show the changes in the localized configurational motifs of the nitrogen with neighboring atoms. It is shown that, excluding the IV-7 CNNT, the total BOs of the selected nitrogen atom covalently connecting three carbon atoms are identified to be around 2.9, indicating their bonding configurational motifs of C(sp^3)-N(sp^2). However, the IV-7 CNNT shows a lower total BOs around 2.6 of the selected nitrogen atom, originating from that it covalently connects with only two carbon atoms. As the elastic elongation is applied, the total BOs of the nitrogen atom in IV-7 insignificantly change. This is explained by that the C-N bonds in IV-7 horizontally covalently links to the carbon chains that effectively absorb the loading energy. However, the total BOs of the selected nitrogen atoms in other CNNTs pronouncedly vary with tension strain because the nitrogen atoms locate at the loading skeleton, similar to the case of carbon atoms. Likewise, the sudden changes in

the total BOs of the nitrogen atoms come from structural transformations of bonding configurations subjected to critical strains. Finally, separation of the CNNTs leads to the deep drop of the total BOs of the nitrogen atoms. Like the case of the selected carbon atom in Polymer I_3-3_25, because of a series of deformation-induced changes in the bonding configurations in the vicinity of the selected nitrogen atom, the selected nitrogen atom is chemically characterized by a uniquely sawtooth-like variation in the total BOs with elongation, corresponding to the long-range sawtooth-shaped mechanical loading curves in Figure 2a.

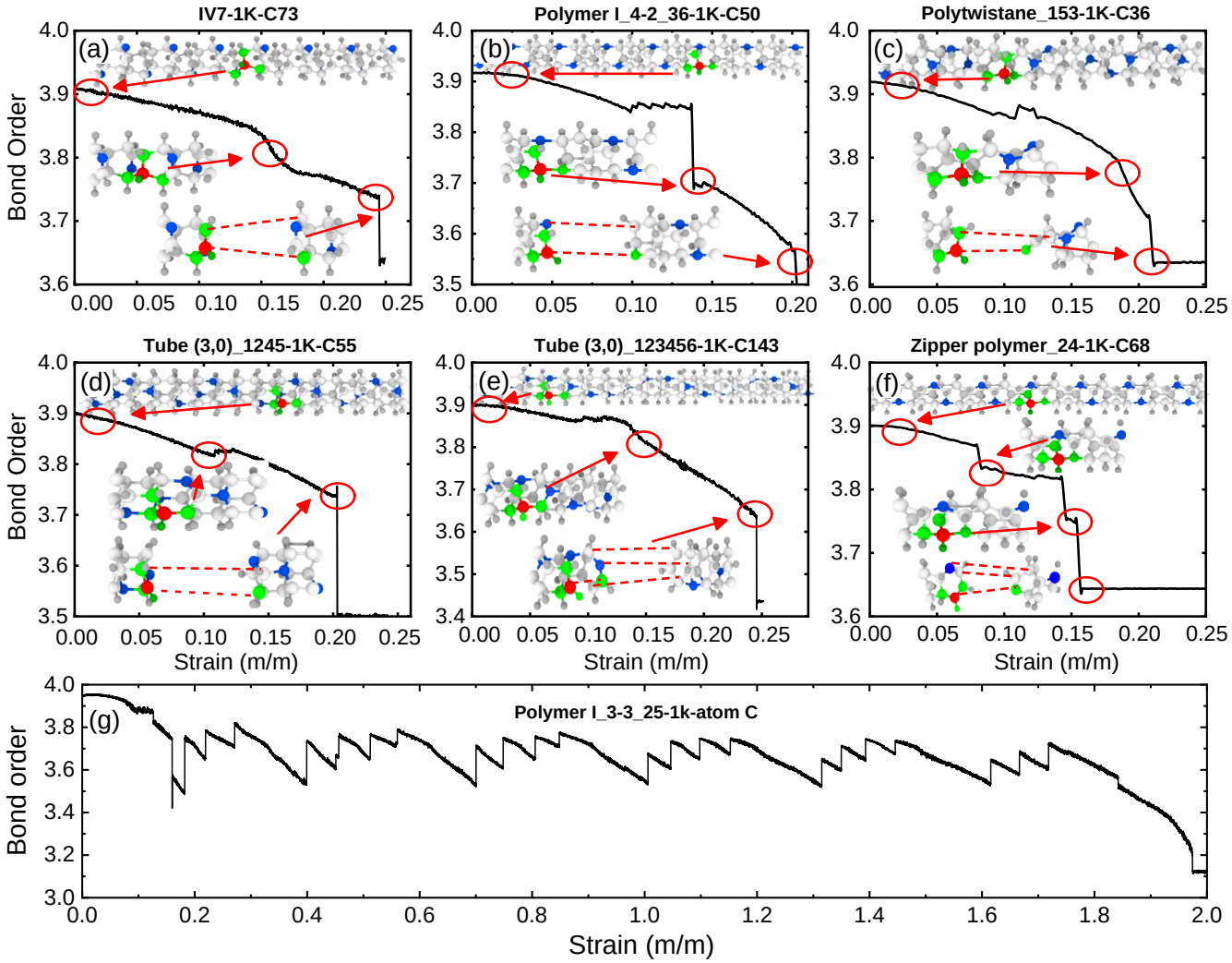

Figure 3 Dynamics of carbon BO of CNNTs subjected to mechanical elongation at low temperature 1 K. (a)-(g) Variation in the total BOs of one carbon atom situated at the failure sites with tension strain for IV-7, Polymer I_4-2_36, Polytwistane_153, Tube (3,0)_1245, Tube (3,0)_123456, Zipper polymer_24 and

Polymer I_3-3_25 CNNTs, respectively. Insets are the snapshots of typical motifs of the carbon with neighboring atoms that are red- and green-highlighted.

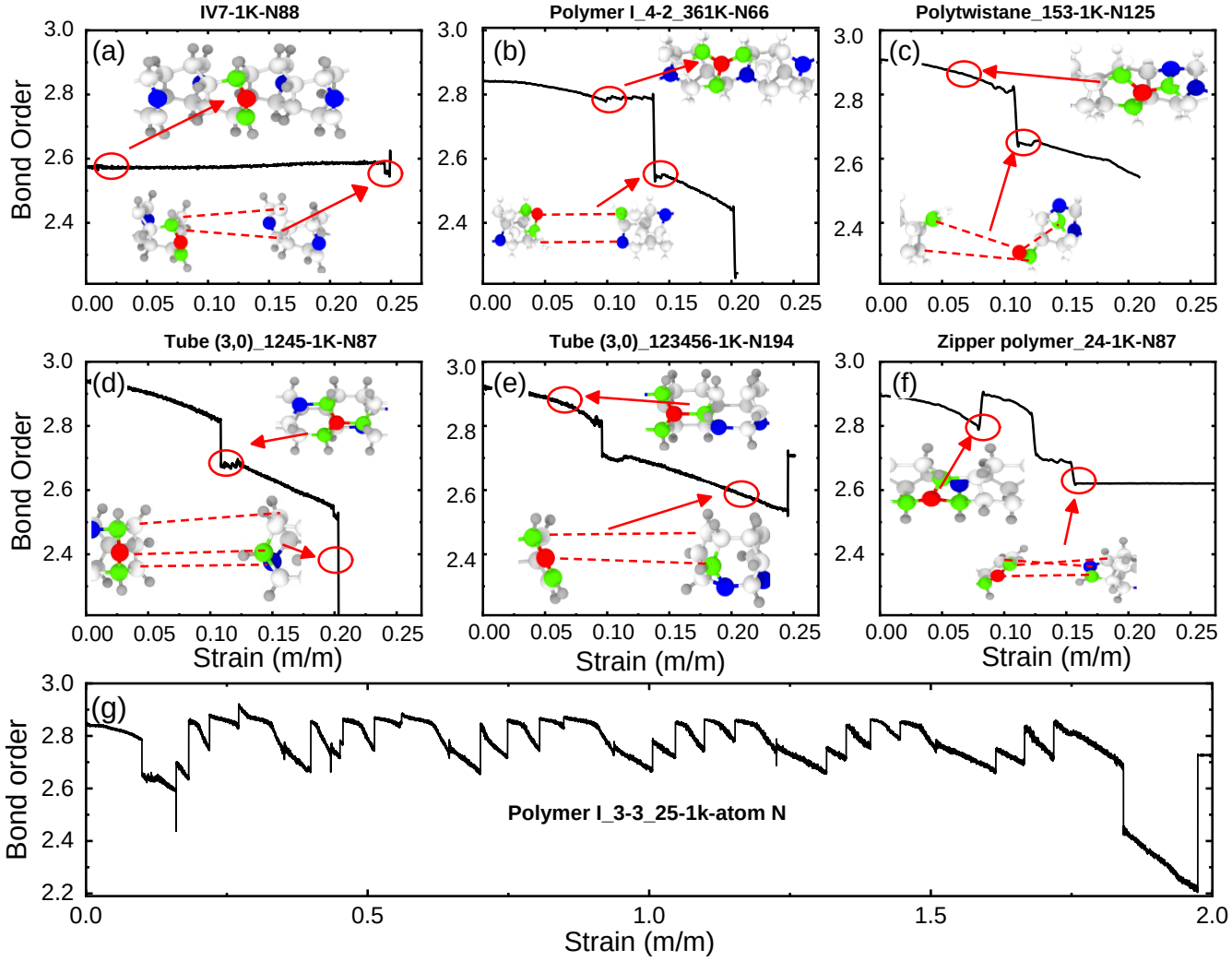

Figure 4 The entire evolution of nitrogen BO of CNNTs under mechanical tension at low temperature 1 K. (a)-(g) Total BOs of one nitrogen atom located at the breaking sites as a function of tension strain for IV-7, Polymer I_4-2_36, Polytwistane_153, Tube (3,0)_1245, Tube (3,0)_123456, Zipper polymer_24 and Polymer I_3-3_25 CNNTs, respectively. Insets show the development of typical motifs of the nitrogen with neighboring atoms.

To capture the chemical bonding information of Polymer I_3-3_25 subjected to extreme elongation, the BOs of both carbon and nitrogen atoms are calculated. Figure 5 compares the developments of BOs of the carbon and nitrogen atoms, and illustrates their chemical BOs changes at different strains. It is shown from

Figure 5a that the total BOs of both selected carbon and nitrogen atoms simultaneously vary during the whole elongation. As is seen from Figure 5b, the chemical BOs of both carbon and nitrogen atoms depend on the environment of location-zone. At zero strain, although atomic positions are identical from crystalline lattice point of view, their slightly different chemical BOs are mainly from their different neighboring atomic distances by thermal fluctuations. As the Polymer I_3-3_25 CNNT is overstretched, chemical BOs of atoms are significantly reduced in the vicinity of breaking sites, resulting from the neighboring environmental changes by dissociation of bonds. For example, the atoms located at the free-stranding single atomic chains and the junctions between the single atomic chain and the CNNT segment hold lower values of chemical BOs. Once the Polymer I_3-3_25 is completely separated, the chemical BOs of fractured single atomic chain rise because the chain is not stretched, as indicated by the snapshots at strains of 1.8 and 2.0

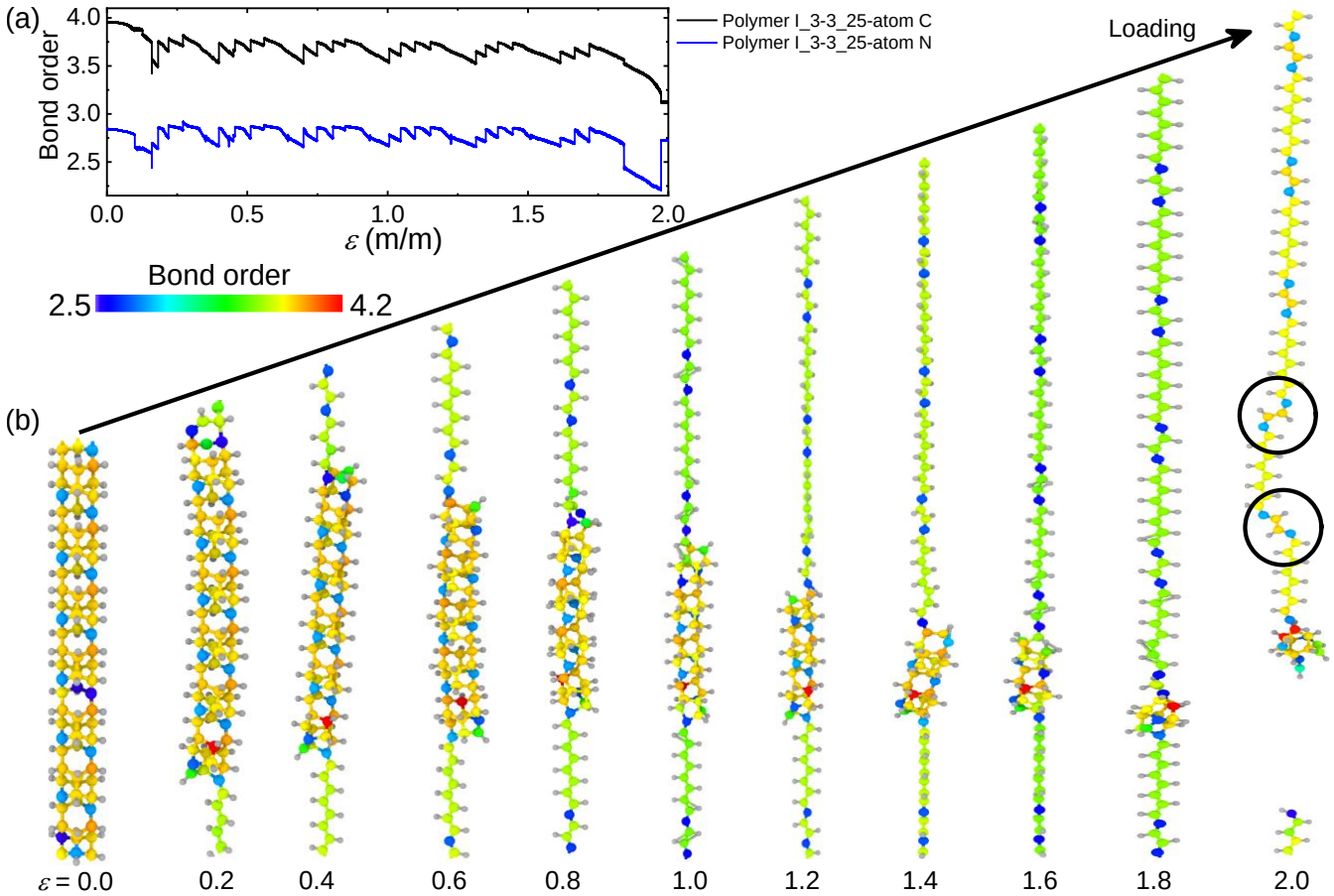

Figure 5 Development of the BOs of Polymer I_3-3_25 CNNT under mechanical deformation at low temperature 1 K. (a) The entire evolution of one carbon and nitrogen BOs during the elongation. (b) Snapshots of the molecular configuration of Polymer I_3-3_25 CNNT at different tension strains, where the carbon and nitrogen atoms are colored based on their BOs.

3.1.3 Brittle versus Ductile at Low Temperature

It is observed that relying on their atomic arrangements, CNNTs are able to show both brittle and ductile fracture characteristics at extremely low temperature 1 K. Polymer I_3-3_25 CNNT shows excellent ductile fracture, whereas other CNNTs exhibit brittle failure. As an example, Figure 6 presents the deformational snapshots of Zipper polymer_24 at different strains to reveal the brittle failure. Apparently, depending on the situation sites of atoms, carbon atoms show distinct chemical BOs although they covalently connect with four atoms. As above-mentioned, Zipper polymer_24 is nature of circular morphology, and thus our investigated Zipper polymer_24 is remarkably pre-strained for maintaining the straight configuration, leading to large range of chemical BOs of atoms. For example, prior to deformation, the values of chemical BOs of the carbon atoms deviate from 3.9. Such non-uniform distribution of chemical BOs indicates distinct mechanical load capacities along the CNNT. It is observed from Figure 6 that, as the tension strain is imposed from 0.0 - 0.1, the chemical BOs of all atoms are reduced as a result of globally straining the bonding configurations. Obviously, when the elongation reaches the strain about 0.14, a significant reduction in localized chemical BOs of both carbon and nitrogen is detected. Once the stretching reaches the critical strain around 0.155, brittle breaking occurs at one cross-section for separating the CNNT, corresponding to the drop of loading stress to zero in the mechanical loading curve. As a result of the relaxation of as-broken CNNT, excluding the separation zone, the atoms nearly recover their initial chemical BOs.

Figure 7 shows the mechanical curve and a series of elongated snapshots of Polymer I_3-3_25 CNNT under extremely axial tension to identify the characteristics of ductile failure. Based on the deformation process, the mechanical stress-strain curve of Polymer I_3-3_25 CNNT is divided into three deformational

stages, where the second deformational stage is uniquely partitioned by 6 sawtooth regions that correspond to ductile failures of repeated atomic configurations under extreme elongation. Figure 7b shows the elastically deformed Polymer I_3-3_25 CNNT composed of seven repeated unit cells of 10C+2N+10H bonding configurations. The unit cell is structurally dominated by a cage made of 4 pentagon rings, and the cages are connected by one C-C and one C-N covalent bonds to form Polymer I_3-3_25 CNNT. To clearly identify the failure characteristics, the carbon and nitrogen atoms in the cages are periodically rendered. Figure 7c presents the configurational snapshots of Polymer I_3-3_25 CNNT that correspond to the dissociation and reformation of covalent bonds in period #1 during deformational stage B. It is observed that Polymer I_3-3_25 CNNT initially fails by two green/red-colored C-C bonds in two pentagonal rings at one cross-section, accompanying with reformation of a C-C bond. This results in the deep drop of the highest peak in Figure 7a and the formation of a polyethene chain composed of three carbon atoms as shown in snapshot #1 in Figure 7c. Afterwards, one C-C and one C-N bonds in another two pentagonal rings dissociate and C-C bond forms, lengthening the polyethene chain with 6 carbon atoms (snapshot #2 in Figure 7c) and resulting in the second drop of loading stress in the period #1 of deformational stage B. The next two dissociations of C-C and C-N bonds in as-failed Polymer I_3-3_25 CNNT occur in two hexagonal rings near the atomic chain, leading to further lengthening of the atomic chain (snapshots #2 and #3) and another two following drops of loading stress in the period #1 of deformational stage B. Figure 7d presents another four configurational snapshots of Polymer I_3-3_25 CNNT, which illustrates the ductile failures of the second unit cell, containing stepwise dissociation and reformation of covalent bonds as indicated by the four peaks in the period #2 during the deformational stage B. Similarly, molecular configuration consisting of another four-unit cell is pronouncedly elongated by a series of fracture vs arrest events, resulting in the following sawtooth stress-strain curves in the deformational stage B. As a result, an extremely long atomic chain is achieved by elongating periodic Polymer I_3-3_25 CNNT composed of multiple unit cells. It is noted that, for the sixth unit cell (period #6), one pentagonal ring does not dissociate, resulting in the three peaks in the mechanical curves. As a

result, before complete separation of Polymer I_3-3_25 CNNT, a unit cell configuration remains non-fracture, as shown in Figure 7e.

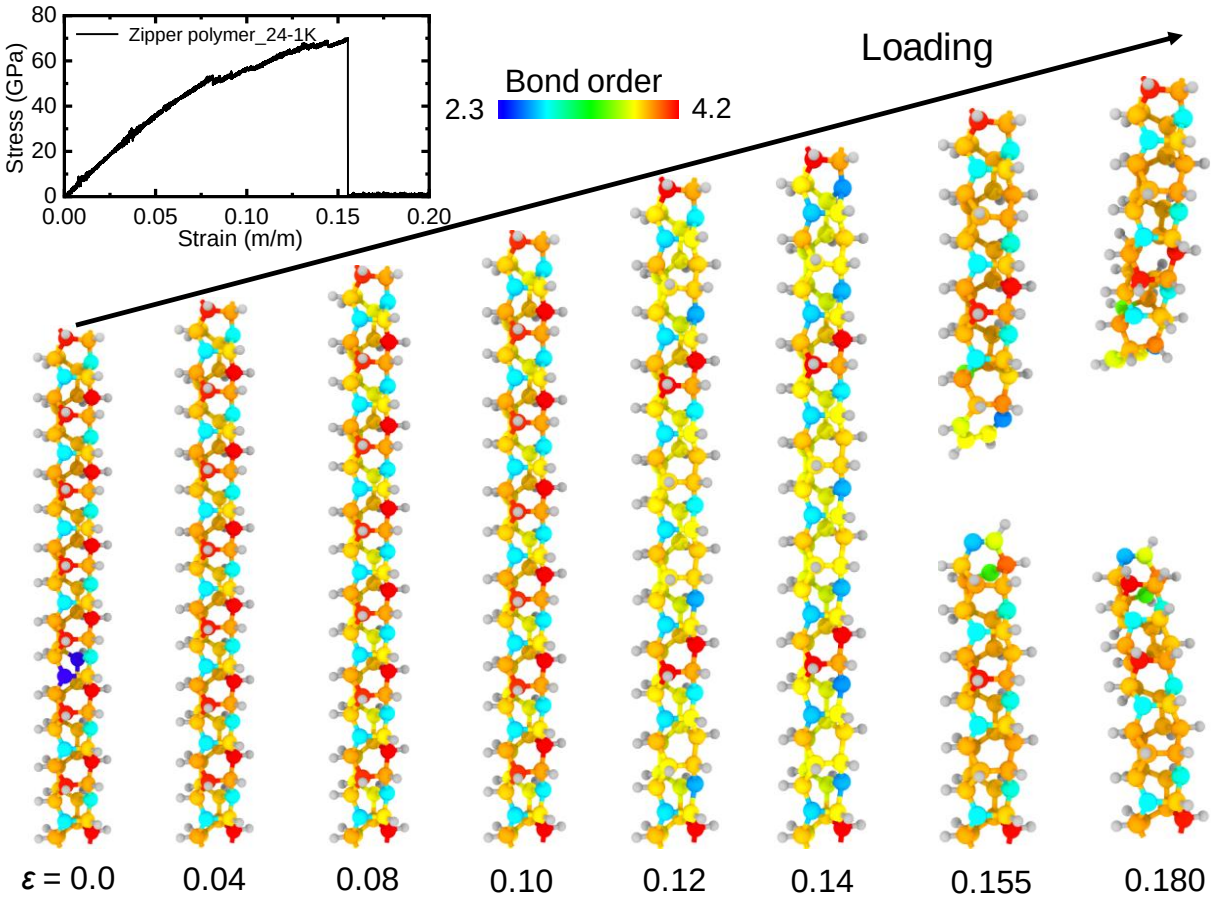

Figure 6 Mechanical response curve and the snapshots of Zipper polymer_24 at different strains, where the atoms are colored on the basis of total chemical BOs.

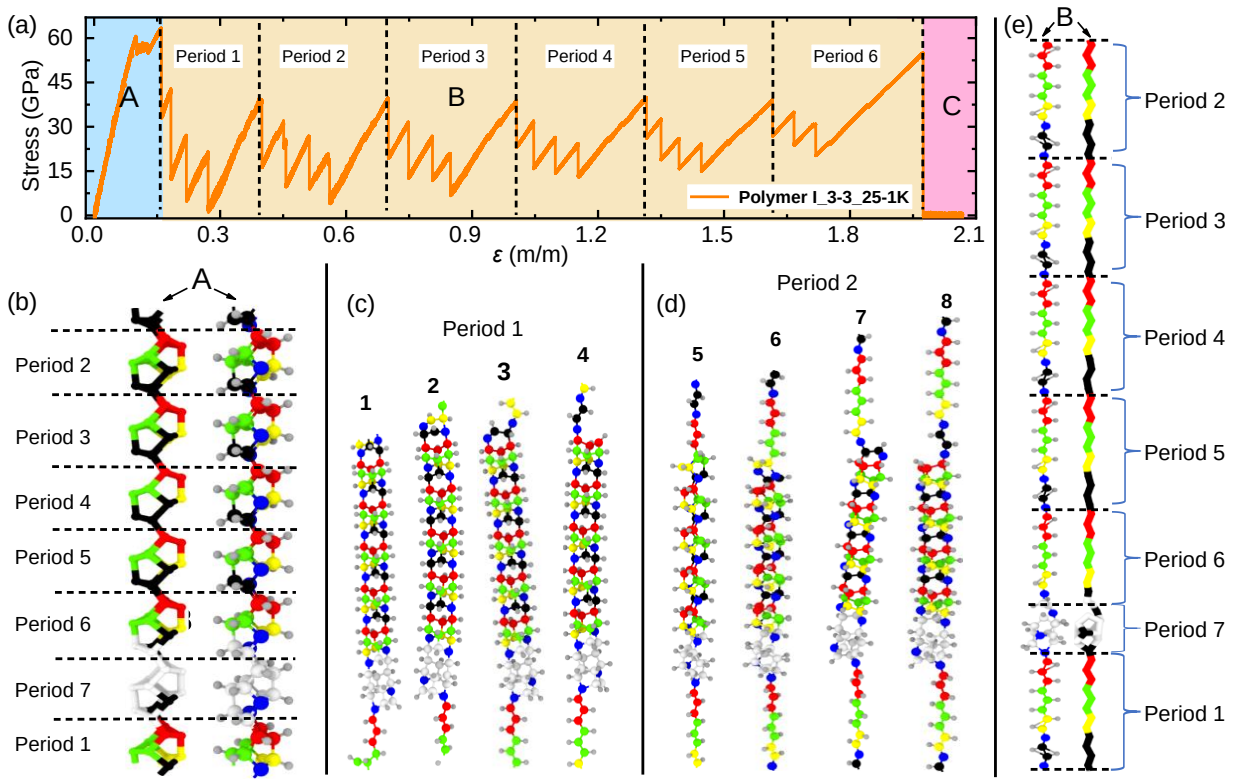

Figure 7 Mechanically elongated characteristics of Polymer I_3-3_25 CNNT. (a) Mechanical loading curve and (b)-(e) a series of configurational snapshots subjected to axial elongation, where the skeleton atoms are differently colored for revealing the characteristics of ductile failure.

3.2 Effects of Temperature on the Tensile Characteristics of CNNTs

3.2.1 Tensile Stress-Strain Curves of CCNTs

Because of the relatively large range and non-uniform distribution of BOs, it is crucial to understand the thermal influences on the elongating properties of the CNNTs. Figure 8 shows the simulated tensile stress-strain curves of the seven CNNTs at temperatures of 1-1500 K. As illustrated in Figure 9, tensile mechanical performance of all the CNNTs is significantly affected by varying the temperature. The mechanical properties are almost degraded as the temperature is increased. Apparently, the elastic nonlinearity is less pronounced with increasing the temperature. As an example, the loading stresses in the intermediate elastic strain strongly oscillate at low temperature, whereas at high temperature the applied

stresses smoothly change with increasing strain. Remarkably, a transition from ductile to brittle failure is identified in Polymer I_3-3_25 CNNT as the temperature is increased from 1 to 100 K, against usual think that covalently organic materials commonly show ductile failures at high temperatures. Such extreme axial stretchability results from uniform distribution of dissociation and reformation of bonds along the CNNT. However, at high temperatures, as a result of thermally-induced atomic vibrations, the reformation of bonds becomes difficult, leading to separation of the CNNT at the fracture-occuring cross-section. To further reveal the finite temperature window for extreme ductile of Polymer I_3-3_25 CNNT, a set of tension MD simulations at low temperatures of 2 K, 5 K, 8 K, 10 K, 12 K, 15 K, 18 K, 20 K, 25 K, 30 K, 50 K, and 80 K have been performed. The resultant tensile stress-strain curves of Polymer I_3-3_25 CNNT at temperatures varying 2 to 80 K are shown in Figure S2. It is observed that, below 15 K, Polymer I_3-3_25 CNNT exhibits extreme tensile ductility as a result of similar plastic deformation as at 1 K. However, above 15 K, it displays very limited elongation (< 25%) due to catastrophically local brittle failure at one cross-section. For the case of other CNNTs, they nearly maintain brittle failures at elevated temperatures under axial tension. This implies that, under extremely low temperature environments, for example, harsh deep space environment, Polymer I_3-3_25 CNNT can find important applications such as mechanically robust sensor, tire, protective suit, energy-absorber, and so on.

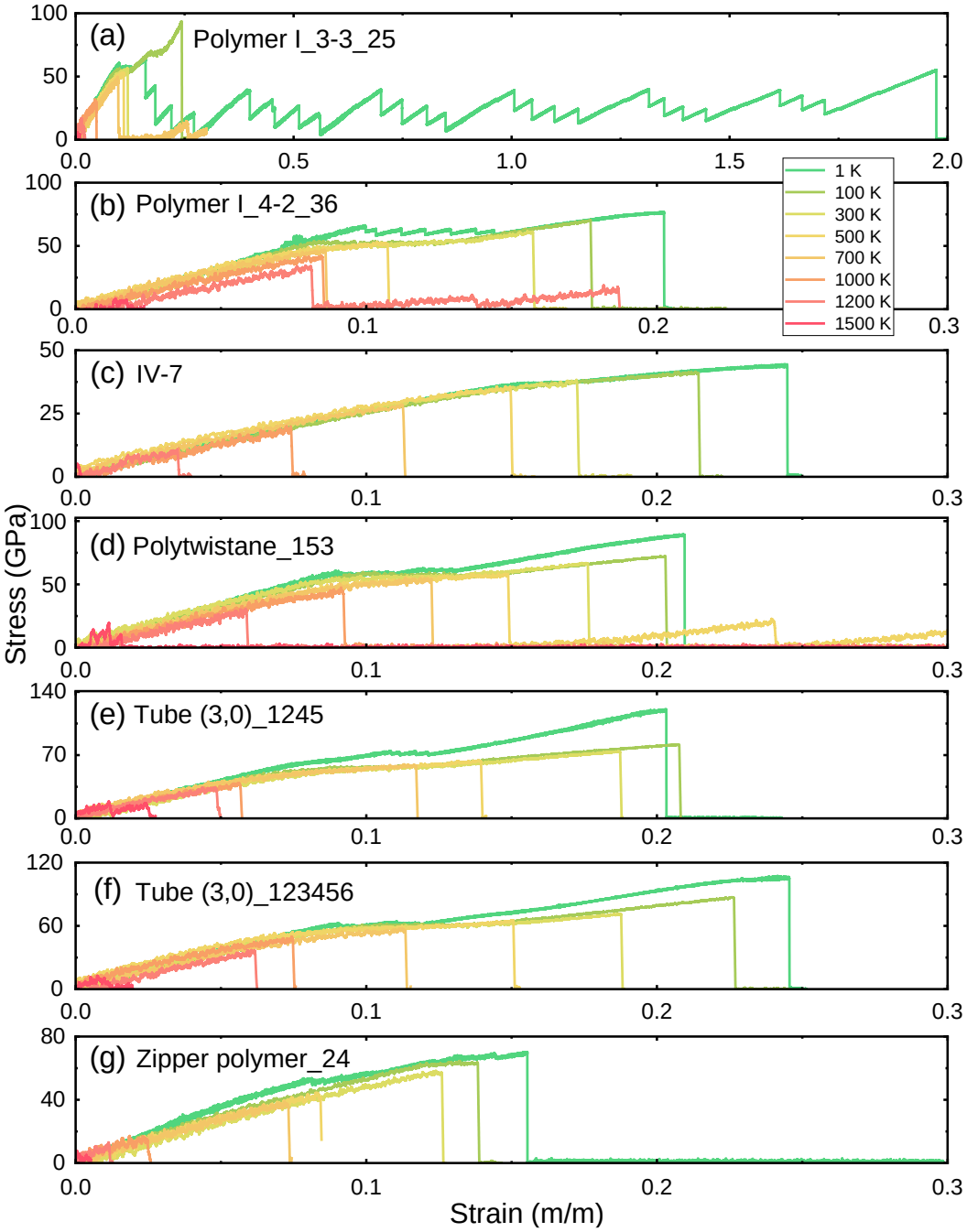

Figure 9 Mechanical performance of CNNTs under temperature ranging from 1-1500 K. (a)-(g) Tensile stress-strain curves of Polymer I_3-3_25, Polymer I_4-2_36, IV-7, Polytwistane_153, Tube (3,0)_1245, Tube (3,0)_123456 and Zipper polymer_24 CNNTs, respectively.

3.2.2 Tensile Properties of CCNTs

The fracture stress and rupture strain as a function of temperature for all the CNNTs are collected from Figure 9 and shown in Figures 10a and 10b, respectively. Obviously, both fracture stress and rupture strain

are markedly affected by the temperature. As is seen, reduction tendencies in the fracture stress of the CNNTs are observed as the temperature is increased from 1K to1500 K. It is found that, in terms of fracture stress, they are differently sorted at 1 and 1500 K, suggesting different thermally-induced reductions in fracture stress. For mechanically robust Tube (3,0)_1245 and Tube (3,0)_123456 CNNTs, the fracture stresses decrease from approximately 120 to 50 GPa and 110 to 40 GPa when the temperature is increased from 1 to 1500 K, with reduction about 58% and 63%, respectively. With regard to the Polymer I_3-3_25, it is interesting to observe that the fracture stress (about 52 GPa) at 1 K is smaller than that at temperatures ranging from 100 to 700 K. For relatively weak IV-7 and Zipper polymer_24 CNNTs, the fracture stresses insignificantly change at low temperatures. As for the rupture strain, as the temperature is increased from 1 to 1500 K, the rupture strains of all the CNNTs are pronouncedly decreased. It is also interesting to identify that the rupture strain of Polymer I_3-3_25 drops from around 200% to 25% when the temperature changes from 1 to 100 K. Unlike the fracture stress and rupture strain, the effective stiffnesses of all the CNNTs are insignificantly dependent on the temperature, similar to the case of DNTs[19, 21].

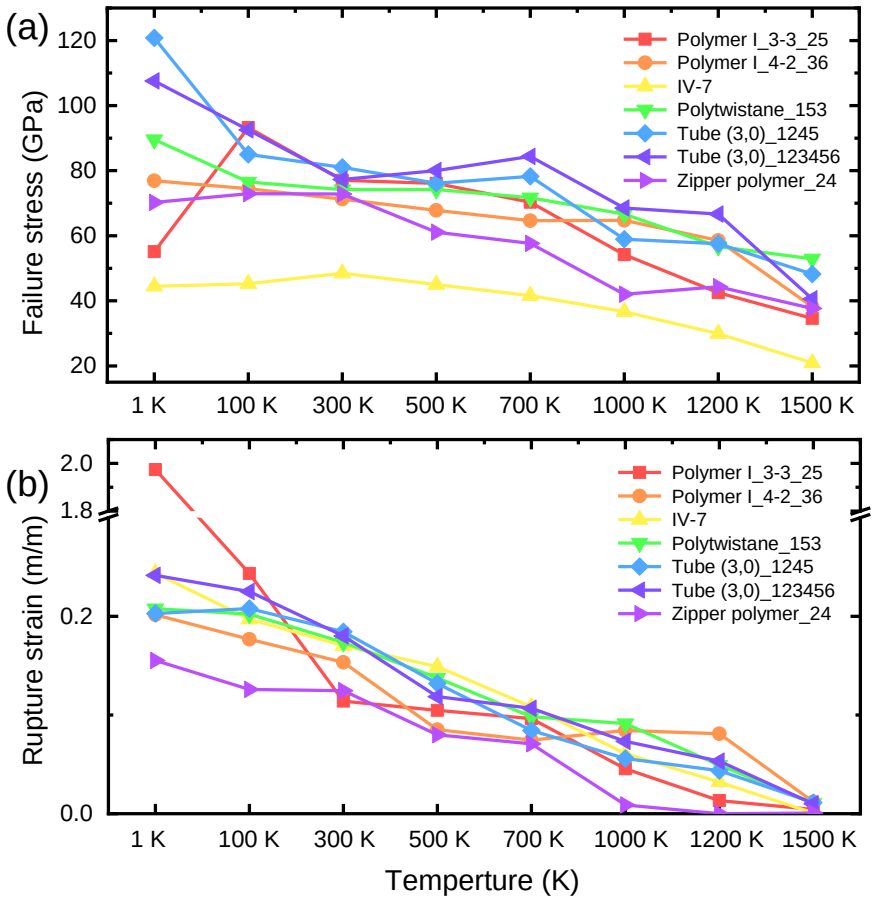

Figure 10 Tensile properties of the seven CNNTs. (a) and (b) Variation in fracture stress and rupture strain as a function of tensile strain.

3.2.2 Effect of Temperature on the Dynamics of BOs and Bond Length in CNNTs

To further understand the temperature-induced mechanical changes of the CNNTs, the variation in the BOs of chemical bond information with axial strain at different temperatures is tracked. Figures 11 and 12 plot the typical relationships of BOs-strain of carbon and nitrogen atoms in mechanically robust Tube (3,0)_1245 CNNT under temperatures varying from 1 K to 1500 K. As expected, the temperature is found to exert a significant effect on the localized chemical BOs. Subjected to elastic elongation at temperature of 1-1500 K, Tube (3,0)_1245 CNNT shows global reduction trend in the chemical BOs of both carbon and nitrogen atoms, although the chemical BOs thermally oscillate. It is observed that there are no obvious deep drops of chemical BOs when the temperature is over 1 K during the elastic deformation. This explains the relatively smooth stress-strain curves under temperature of over 1 K in Figure 9. At higher temperatures,

elastic strain-induced change in chemical BOs is less significant. As the Tube (3,0)_1245 CNNT fails by covalent bond dissociations at different temperature, the chemical BOs are suddenly significantly changed. With regard to other CNNTs, similar effect of temperature on the localized chemical BOs is revealed as seen in Figure S3-S14. Moreover, the variations in specif bond length in the backbone of CNNTs with axial strain at different temperatures were also traced and shown in Figure S15-S21. It is found that all CNNTs show nonlinear behaviors in the relationship between bond length-strain. Detail discussion can be found in Supporting Information.

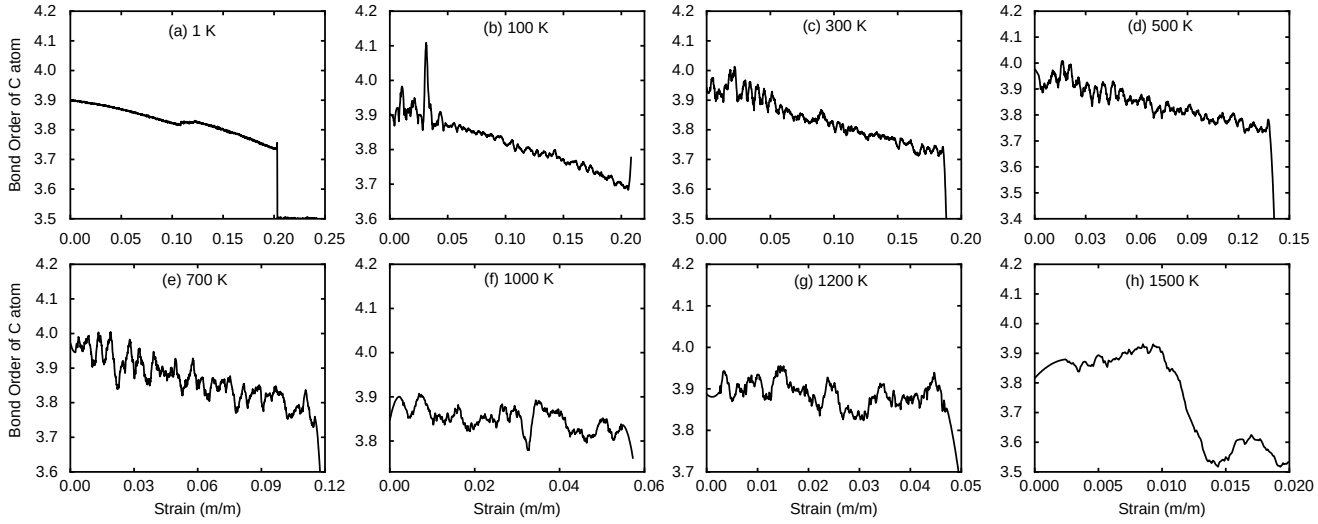

Figure 11 Dynamics of BOs of Tube (3,0)_1245 CNNT subjected to elongation. (a)-(h) Variation in the chemical BOs of one carbon atom with axial strain at temperatures varying from 1-1500 K.

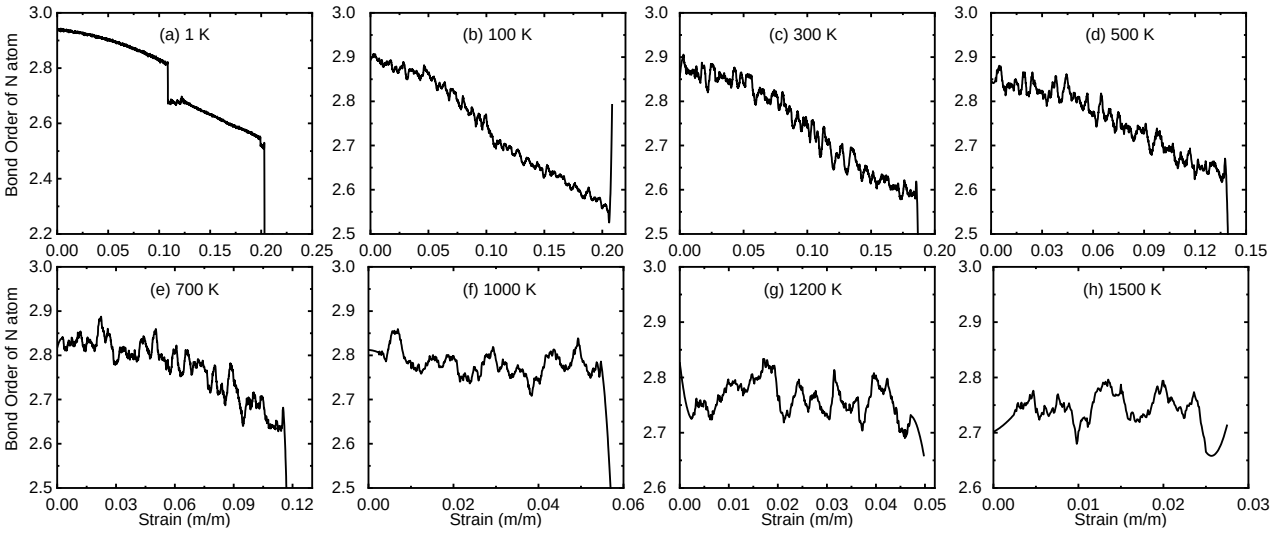

Figure 12 Dynamics of BOs of Tube (3,0)_1245 CNNT subjected to elongation. (a)-(h) Variation in the chemical BOs of one nitrogen atom with axial strain at temperatures varying from 1-1500 K.

4 Conclusions

In summary, mechanical characteristics of seven experimental achieved CNNTs are systemically investigated by using MD simulations with Reaxff forcefield. It is revealed that the tensile properties of CNNTs can vary pronouncedly because of distinct differences in the molecular morphology, atomic arrangement and the distribution of nitrogen atoms in the loading skeleton. For example, CNNTs with diamond-like atomic structures exhibit outperformance of Young's modulus and fracture strength over other CNNTs. Notably, Zipper polymer_24 with inherently circular morphology shows high effective stiffness but low fracture strength because it is pre-strained for its linear configuration. Polymer I_3-3_25 and Polymer I_4-2_36 CNNTs with identical element atoms but different distribution of nitrogen atoms along the skeleton show distinct tensile characteristics; Polymer I_3-3_25 is able to be extremely elongated to form linear polymer at 1 K as a result of 4-step dissociation-and-reformation of bonds in repeated unit structures of $5^4 6^2$ cage, whereas Polymer I_4-2_36 CNNT is finitely stretched due to dissociation of bonds at one cross-section. However, at higher temperatures, the Polymer I_3-3_25 CNNT shows brittle failure with low ductility similar to other CNNTs. It is found that temperature has a strong effect on the fracture strength and rupture strain, but not for the effective tensile stiffness. Generally, the values of atomic BOs nonlinearly reduce with increasing axial strain, explaining the nonlinearity in the tensile stress-strain curves. Moreover, subject to elastic elongation, the bonds in the skeleton of CNNTs are also nonlinearly lengthened with increasing axial strain, and the nonlinearities of bond length-strain curves are strongly dependent on the molecular morphology. This again explains the morphology dependent tensile responses of CNNTs. The fundamental knowledge of tensile mechanical characteristics of CNNTs is critically significant for design and application of CNNTs as a promising building block for the next generation of mechanical devices[46] and multifunctional materials[47]. Specially, we predict that Polymer I_3-3_25 CNNT can be used widely in ultra-low temperature environment, with its outstanding ductile performance.

Acknowledgments

This work is financially supported by the National Natural Science Foundation of China (Grant Nos. 11772278 and 11502221), the Jiangxi Provincial Outstanding Young Talents Program (Grant Nos. 20192BCBL23029), the Fundamental Research Funds for the Central Universities (Xiamen University: Grant Nos. 20720180014, 20720180018 and 20720160088), Fujian Provincial Department of Science & Technology (2017J05028), "111" Project (B16029) and the 1000 Talents Program from Xiamen University, the Chinese Scholarship Council, and the Research Council of Norway (Grant No.251068). The computational resources were provided by the Norwegian Metacenter for Computational Science (NOTUR NN9110K and NN9391K).

References

1. T. Hyeon, S. Han, Y. E. Sung, K. W. Park and Y. W. Kim, *Angewandte Chemie International Edition*, 2003, **42**, 4352-4356.
2. S. Iijima, *nature*, 1991, **354**, 56.
3. J. Zhang, M. Terrones, C. R. Park, R. Mukherjee, M. Monthioux, N. Koratkar, Y. S. Kim, R. Hurt, E. Frackowiak and T. Enoki, *Carbon*, 2016, **98**, 708-732.
4. T. C. Fitzgibbons, M. Guthrie, E. S. Xu, V. H. Crespi, S. K. Davidowski, G. D. Cody, N. Alem and J. V. Badding, *Nat Mater*, 2015, **14**, 43-47.
5. H. Zhan, G. Zhang, V. B. Tan, Y. Cheng, J. M. Bell, Y. W. Zhang and Y. Gu, *Advanced Functional Materials*, 2016, **26**, 5279-5283.
6. N. Yang, H. Uetsuka, E. Osawa and C. E. Nebel, *Angewandte Chemie International Edition*, 2008, **47**, 5183-5185.
7. H. Zhan, G. Zhang, V. B. Tan and Y. Gu, *Nat Commun*, 2017, **8**, 14863.
8. H. Zhan, G. Zhang, V. B. Tan, Y. Cheng, J. M. Bell, Y. W. Zhang and Y. Gu, *Nanoscale*, 2016, **8**, 11177-11184.
9. W. Smirnov, A. Kriele, R. Hoffmann, E. Sillero, J. Hees, O. A. Williams, N. Yang, C. Kranz and C. E. Nebel, *Anal Chem*, 2011, **83**, 4936-4941.
10. K. Duan, J. Zhang, L. Li, Y. Hu, W. Zhu and X. Wang, *Composites Science and Technology*, 2019, **174**, 84-93.
11. L. A. Openov and A. I. Podlivaev, *JETP Letters*, 2016, **104**, 193-196.
12. P. Duan, X. Li, T. Wang, B. Chen, S. J. Juhl, D. Koeplinger, V. H. Crespi, J. V. Badding and K. Schmidt-Rohr, *J Am Chem Soc*, 2018, **140**, 7658-7666.
13. X. Li, M. Baldini, T. Wang, B. Chen, E. S. Xu, B. Vermilyea, V. H. Crespi, R. Hoffmann, J. J. Molaison, C. A. Tulk, M. Guthrie, S. Sinogeikin and J. V. Badding, *J Am Chem Soc*, 2017, **139**, 16343-16349.
14. K. Mylvaganam and L. Zhang, *Carbon*, 2004, **42**, 2025-2032.
15. S. Frankland, V. Harik, G. Odegard, D. Brenner and T. Gates, *Composites Science and Technology*, 2003, **63**, 1655-1661.
16. R. E. Roman, K. Kwan and S. W. Cranford, *Nano letters*, 2015, **15**, 1585-1590.
17. E.-s. Xu, P. E. Lammert and V. H. Crespi, *Nano letters*, 2015, **15**, 5124-5130.
18. H. Zhan, G. Zhang, V. B. Tan, Y. Cheng, J. M. Bell, Y.-W. Zhang and Y. Gu, *Nanoscale*, 2016, **8**, 11177-11184.
19. H. Zhan, G. Zhang, J. M. Bell and Y. Gu, *Carbon*, 2016, **107**, 304-309.
20. R. E. Roman, K. Kwan and S. W. Cranford, *Nano Lett*, 2015, **15**, 1585-1590.
21. C. Feng, J. Xu, Z. Zhang and J. Wu, *Carbon*, 2017, **124**, 9-22.

22. J. F. R. V. Silveira and A. R. Muniz, *Carbon*, 2017, **113**, 260-265.
23. J. F. Silveira and A. R. Muniz, *Phys Chem Chem Phys*, 2017, **19**, 7132-7137.
24. B. J. M. Hausmann, T. M. Babinec, J. T. Choy, J. S. Hodges, S. Hong, I. Bulu, A. Yacoby, M. D. Lukin and M. Lončar, *New Journal of Physics*, 2011, **13**.
25. Q. Wang, P. Subramanian, M. Li, W. S. Yeap, K. Haenen, Y. Coffinier, R. Boukherroub and S. Szunerits, *Electrochemistry Communications*, 2013, **34**, 286-290.
26. Y. Yu, L. Wu and J. Zhi, *Angew Chem Int Ed Engl*, 2014, **53**, 14326-14351.
27. H. Zhan, G. Zhang, V. B. C. Tan, Y. Cheng, J. M. Bell, Y.-W. Zhang and Y. Gu, *Advanced Functional Materials*, 2016, **26**, 5279-5283.
28. X. Li, T. Wang, P. Duan, M. Baldini, H. T. Huang, B. Chen, S. J. Juhl, D. Koeplinger, V. H. Crespi, K. Schmidt-Rohr, R. Hoffmann, N. Alem, M. Guthrie, X. Zhang and J. V. Badding, *J Am Chem Soc*, 2018, **140**, 4969-4972.
29. P. G. Demingos and A. R. Muniz, *The Journal of Physical Chemistry C*, 2019, **123**, 3886-3891.
30. E. S. Xu, P. E. Lammert and V. H. Crespi, *Nano Lett*, 2015, **15**, 5124-5130.
31. T. Wang, P. Duan, E.-S. Xu, B. Vermilyea, B. Chen, X. Li, J. V. Badding, K. Schmidt-Rohr and V. H. Crespi, *Nano letters*, 2018, **18**, 4934-4942.
32. B. Chen, T. Wang, V. H. Crespi, X. Li, J. Badding and R. Hoffmann, *J Chem Theory Comput*, 2018, **14**, 1131-1140.
33. X. Li, M. Baldini, T. Wang, B. Chen, E.-s. Xu, B. Vermilyea, V. H. Crespi, R. Hoffmann, J. J. Molaison and C. A. Tulk, *Journal of the American Chemical Society*, 2017, **139**, 16343-16349.
34. B. Chen, T. Wang, V. H. Crespi, X. Li, J. Badding and R. Hoffmann, *Journal of chemical theory and computation*, 2018, **14**, 1131-1140.
35. A. C. Van Duin, S. Dasgupta, F. Lorant and W. A. Goddard, *The Journal of Physical Chemistry A*, 2001, **105**, 9396-9409.
36. T. P. Senftle, S. Hong, M. M. Islam, S. B. Kylasa, Y. Zheng, Y. K. Shin, C. Junkermeier, R. Engel-Herbert, M. J. Janik, H. M. Aktulga, T. Verstraelen, A. Grama and A. C. T. van Duin, *npj Computational Materials*, 2016, **2**.
37. H. Zhao, Q. Shi, Z. Han, H. Gong, Z. Zhang, S. Wu and J. Wu, *Carbon*, 2018, **138**, 243-256.
38. C. Sui, Y. Zhao, Z. Zhang, J. He, Z. Zhang, X. He, C. Wang and J. Wu, *ACS Omega*, 2017, **2**, 3977-3988.
39. J. M. de Sousa, T. Botari, E. Perim, R. A. Bizao and D. S. Galvao, *RSC Advances*, 2016, **6**, 76915-76921.
40. J. Budzien, A. P. Thompson and S. V. Zybin, *The Journal of Physical Chemistry B*, 2009, **113**, 13142-13151.
41. J. Wu, J. He, G. M. Odegard, S. Nagao, Q. Zheng and Z. Zhang, *Journal of the American Chemical Society*, 2013, **135**, 13775-13785.
42. X. Chen, S. Zhang, D. A. Dikin, W. Ding, R. S. Ruoff, L. Pan and Y. Nakayama, *Nano Letters*, 2003, **3**, 1299-1304.
43. J. Wu, S. Nagao, J. He and Z. Zhang, *Small*, 2013, **9**, 3561-3566.
44. T. Miller, A. B. Jorge, T. Suter, A. Sella, F. Cora and P. McMillan, *Physical Chemistry Chemical Physics*, 2017, **19**, 15613-15638.
45. M. S. Dresselhaus, G. Dresselhaus and P. C. Eklund, *Science of fullerenes and carbon nanotubes: their properties and applications*, Elsevier, 1996.
46. A. Bianco, Y. Chen, Y. Chen, D. Ghoshal, R. H. Hurt, Y. A. Kim, N. Koratkar, V. Meunier and M. Terrones, *Carbon*, 2018, **132**, 785-801.
47. A. L. Antaris, J. T. Robinson, O. K. Yaghi, G. Hong, S. Diao, R. Luong and H. Dai, *ACS nano*, 2013, **7**, 3644-3652.

Supporting Information

Effects of Morphology and Temperature on the Tensile Characteristics of Carbon Nitride Nanothreads

Yuequn Fu,[a] Ke Xu,[b] Jianyang Wu, [*ab] Zhiliang Zhang[a] and Jianying He[*a]

[a]NTNU Nanomechanical Lab, Norwegian University of Science and Technology (NTNU), Trondheim 7491, Norway

[b]Department of Physics, Research Institute for Biomimetics and Soft Matter, Jiujiang Research Institute and Fujian Provincial Key Laboratory for Soft Functional Materials Research, Xiamen University, Xiamen 361005, PR China

[*]Corresponding Emails: jianyang@xmu.edu.cn, jianying.he@ntnu.no

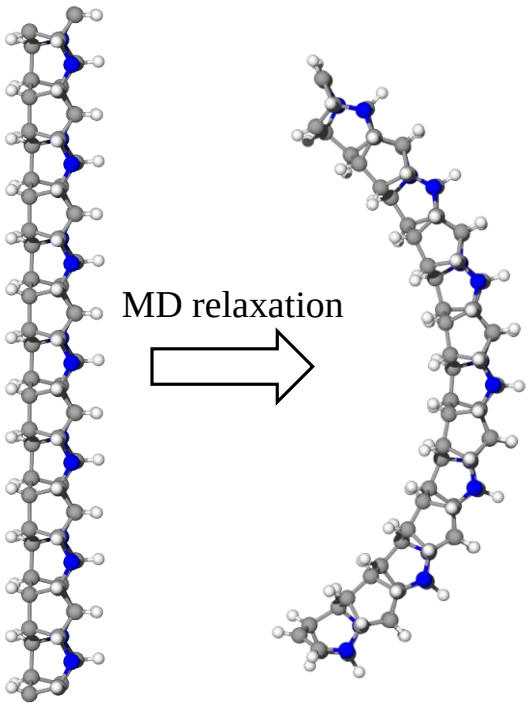

Figure S1 Configurational motif of a segment of Zipper polymer_24 after fully MD relaxiation.

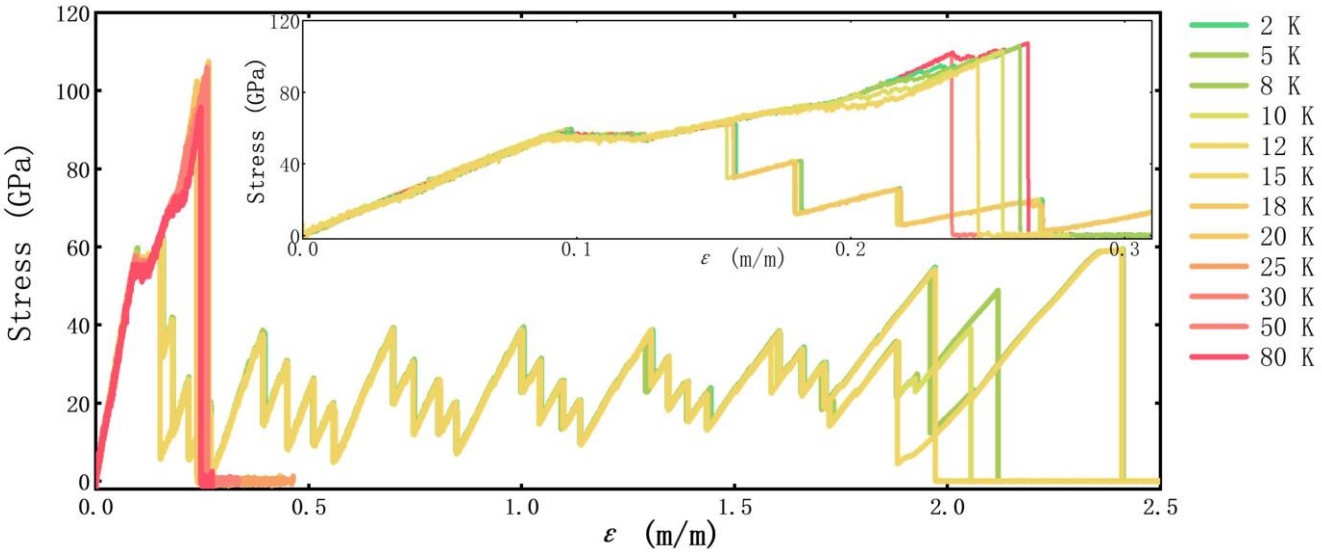

Figure S2 Mechanical performance of Polymer I_3-3_25 CNNT under temperature ranging from 2-80 K. The insert shows the stress-strain curves at small scale deformation.

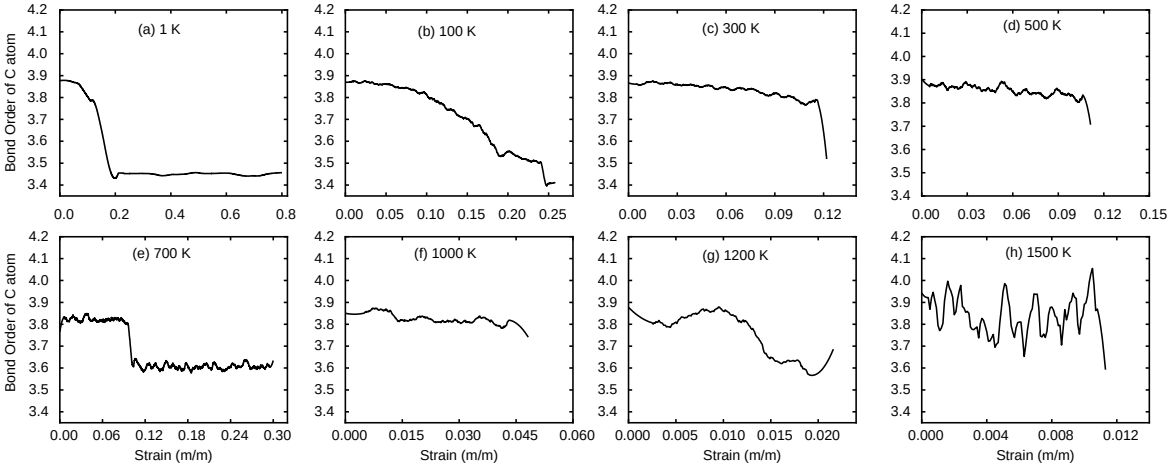

Figure S3 (a)-(h) Variation in the chemical BOs of one carbon atom with globally axial strain for Polymer I_3-3_25 at temperature from 1-1500 K, respectively.

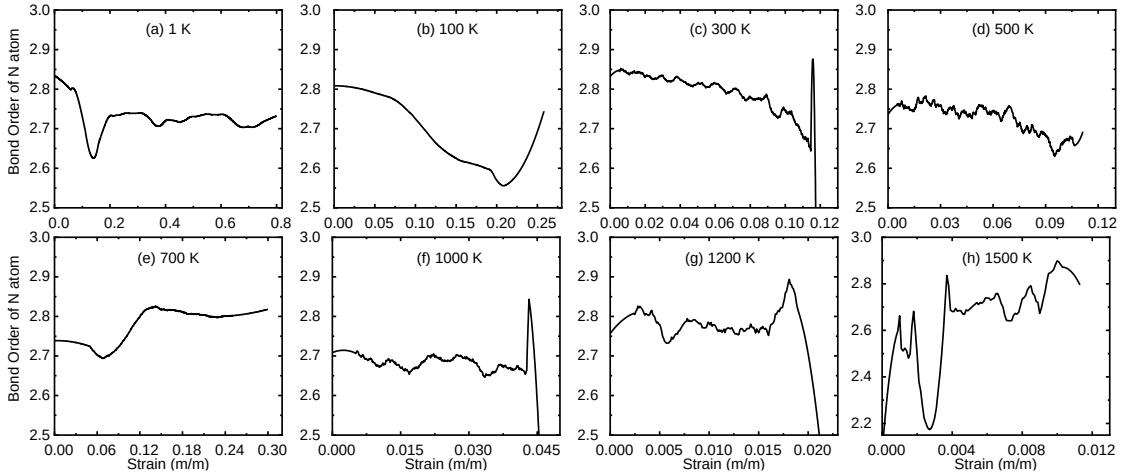

Figure S4 (a)-(h) Variation in the chemical BOs of one nitrogen atom with globally axial strain for Polymer I_3-3_25 at temperature from 1-1500 K, respectively.

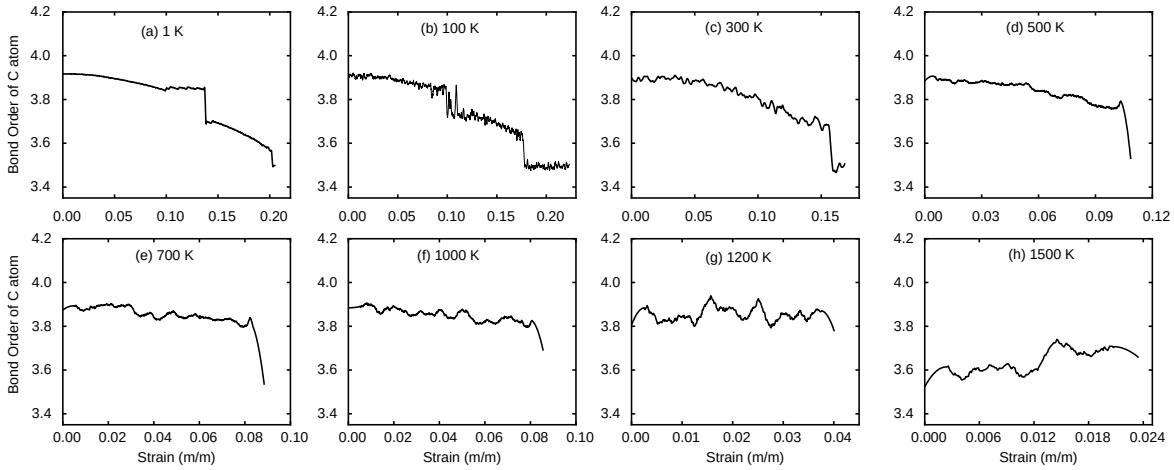

Figure S5 (a)-(h) Variation in the chemical BOs of one carbon atom with globally axial strain for Polymer I_4-2_36 at temperature from 1-1500 K, respectively.

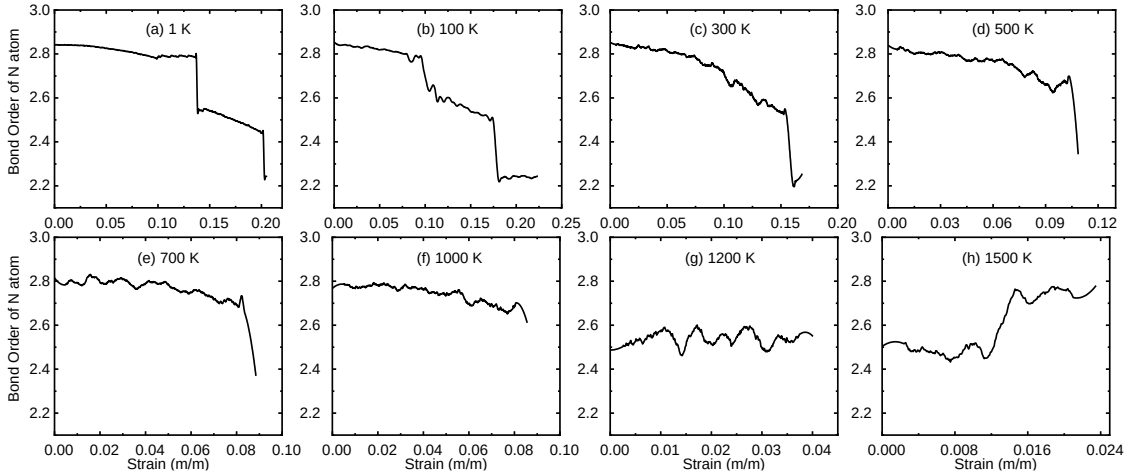

Figure S6 (a)-(h) Variation in the chemical BOs of one nitrogen atom with globally axial strain for Polymer I_4-2_36 at temperature from 1-1500 K, respectively.

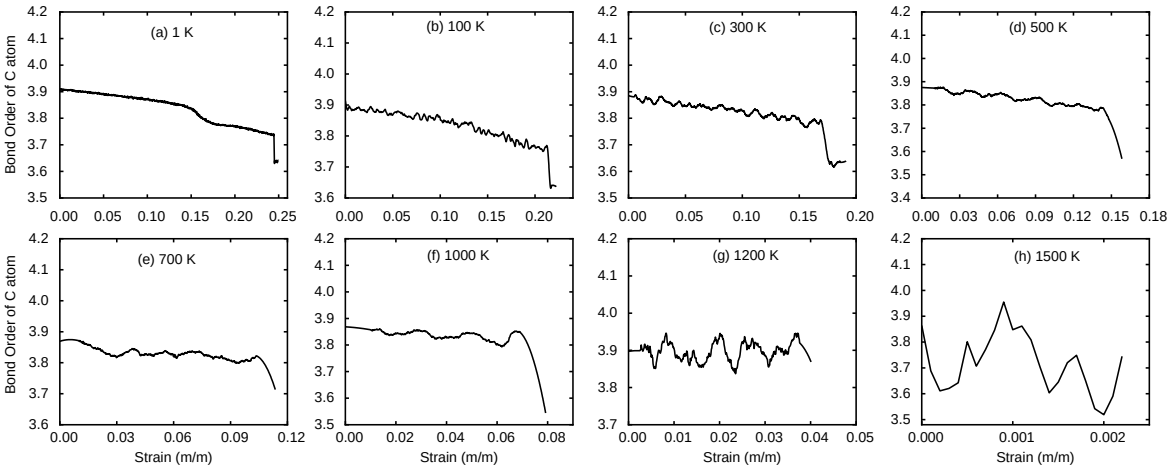

Figure S7 (a)-(h) Variation in the chemical BOs of one carbon atom with globally axial strain for IV-7 at temperature from 1-1500 K, respectively.

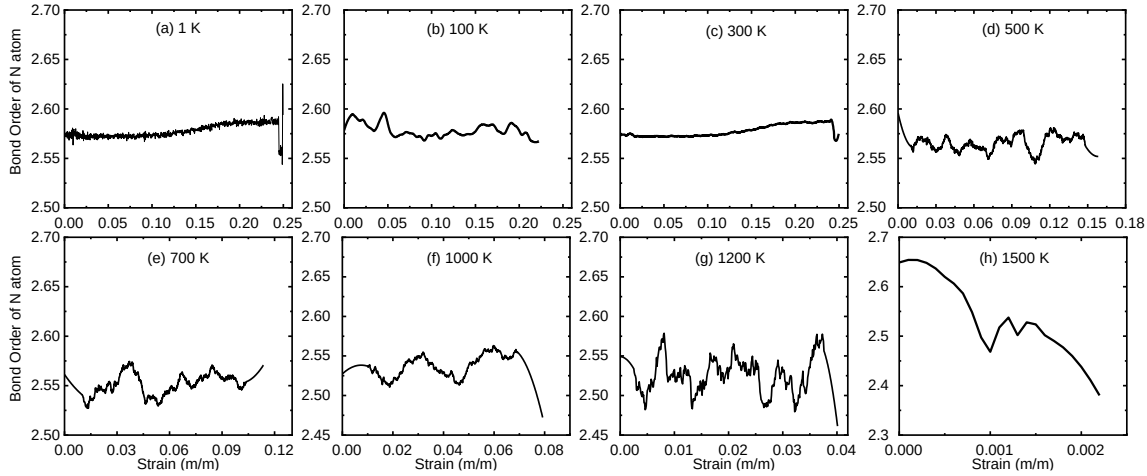

Figure S8 (a)-(h) Variation in the chemical BOs of one nitrogen atom with globally axial strain for IV-7 at temperature from 1-1500 K, respectively.

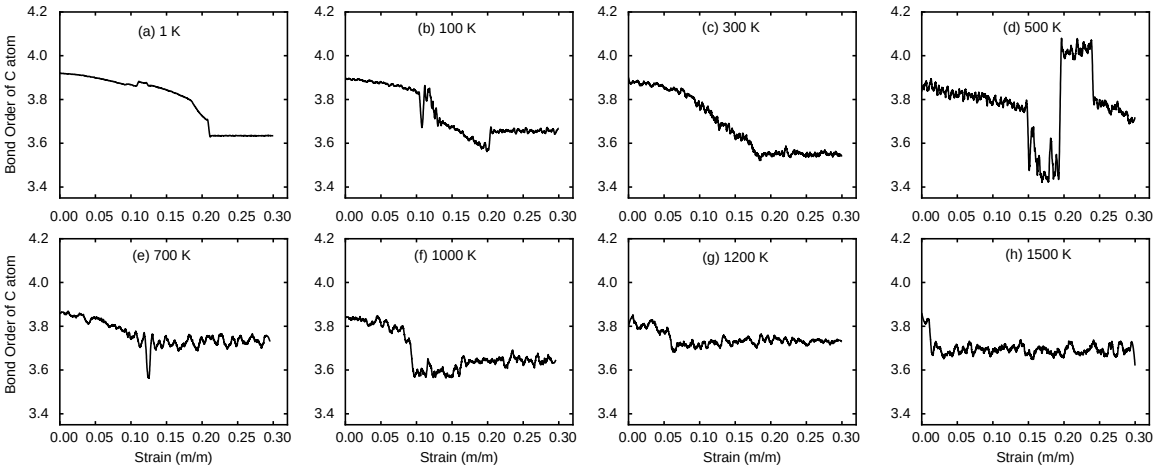

Figure S9 (a)-(h) Variation in the chemical BOs of one carbon atom with globally axial strain for Polytwistane_153 at temperature from 1-1500 K, respectively.

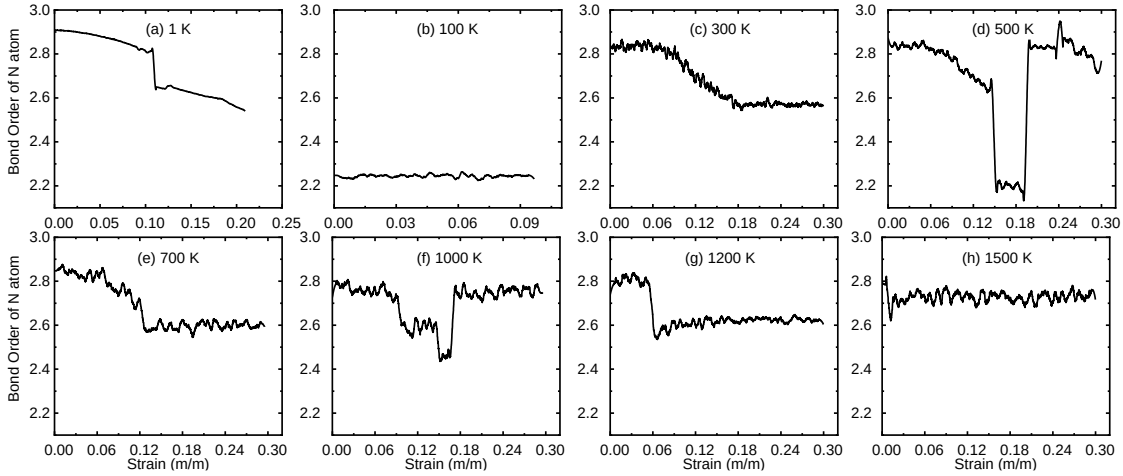

Figure S10 (a)-(h) Variation in the chemical BOs of one nitrogen atom with globally axial strain for Polytwistane_153 at temperature from 1-1500 K, respectively.

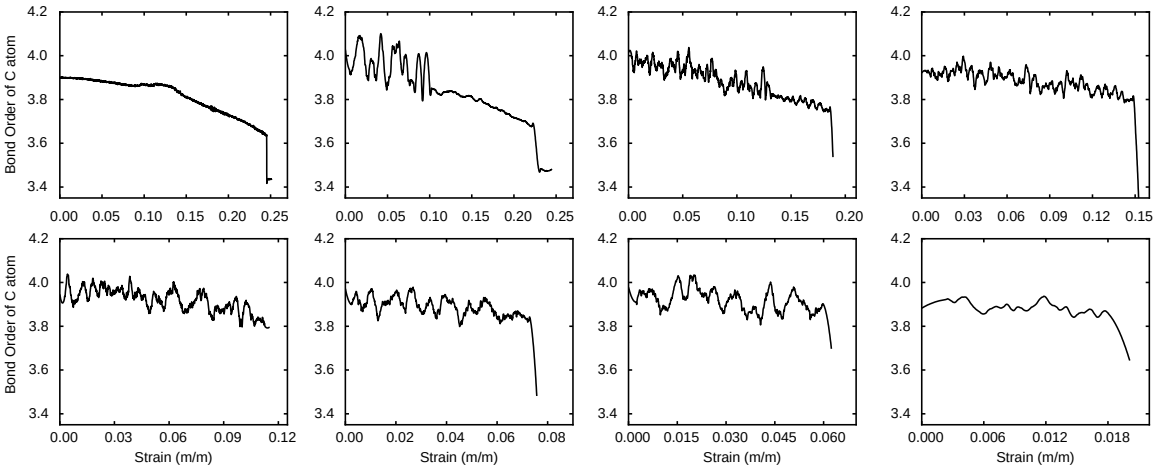

Figure S11 (a)-(h) Variation in the chemical BOs of one carbon atom with globally axial strain for Tube (3,0)_123456 at temperature from 1-1500 K, respectively.

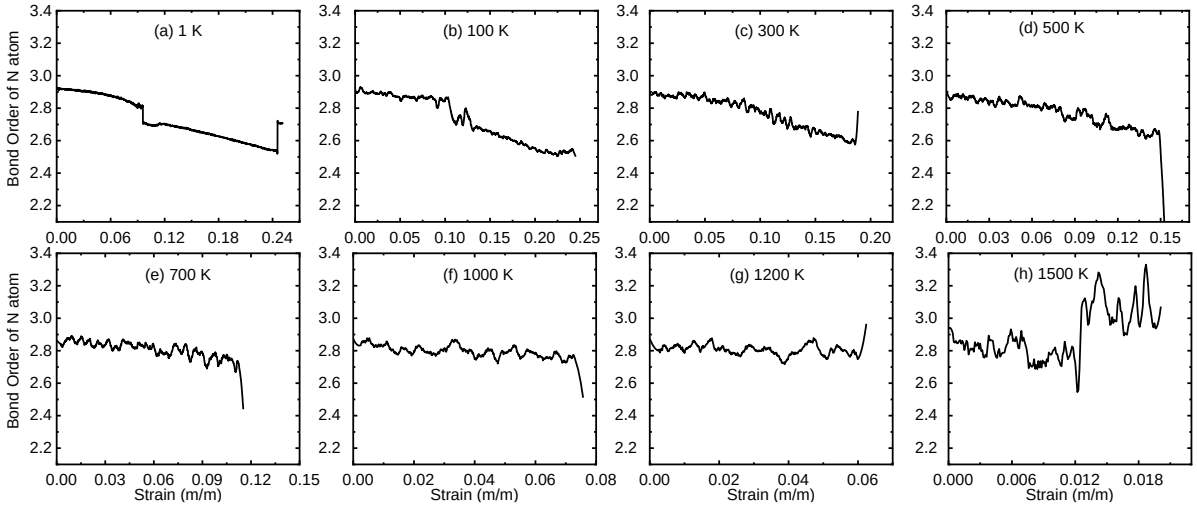

Figure S12 (a)-(h) Variation in the chemical BOs of one nitrogen atom with globally axial strain for Tube (3,0)_123456 at temperature from 1-1500 K, respectively.

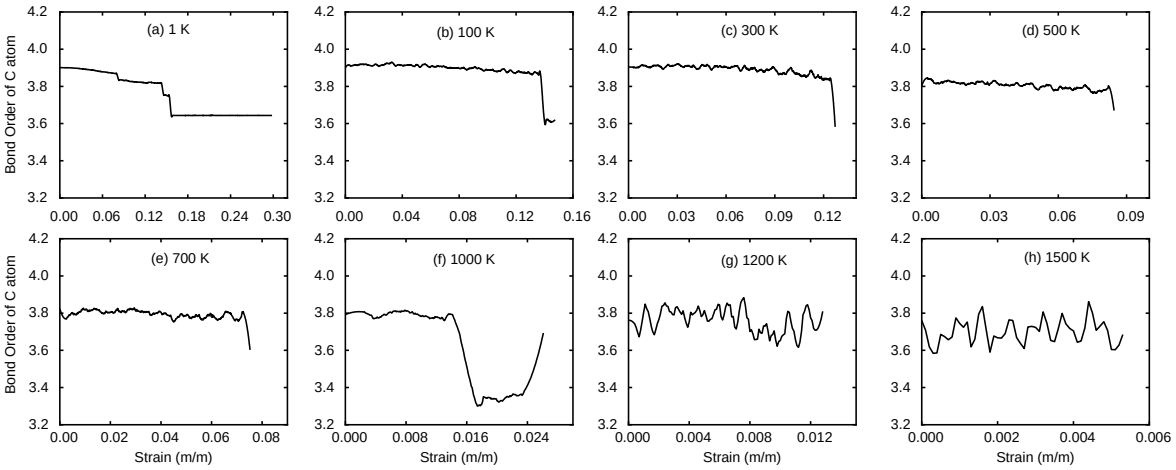

Figure S13 (a)-(h) Variation in the chemical BOs of one carbon atom with globally axial strain for Zipper polymer_24 at temperature from 1-1500 K, respectively.

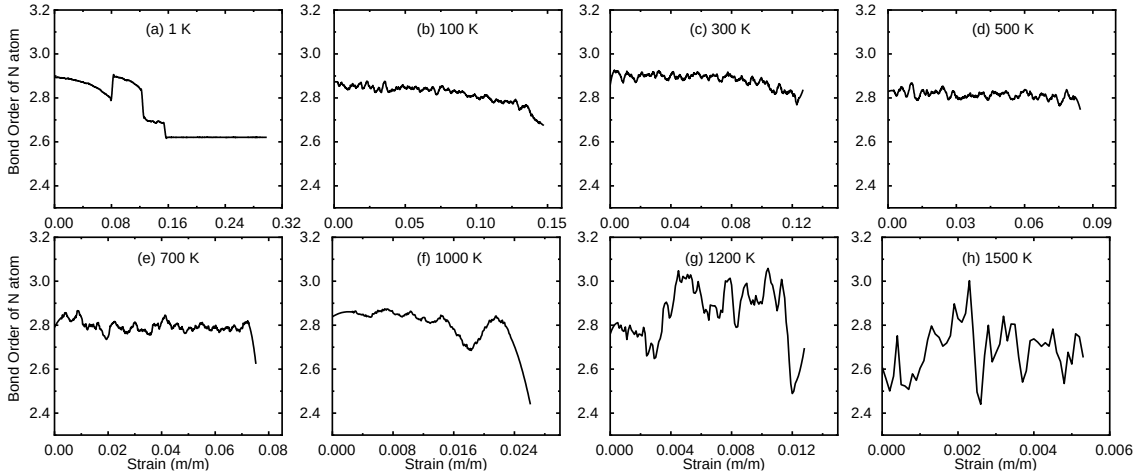

Figure S14 (a)-(h) Variation in the chemical BOs of one nitrogen atom with globally axial strain for Zipper polymer_24 at temperature from 1-1500 K, respectively.

Dynamics of Bond Length in CNNTs

Failure of CNNTs by axial elongation is mainly characterized by deformation-induced dissociation of localized covalent bonds. Elongation development of localized bonds is therefore monitored to

understand the deformation mechanisms. Figure S15 shows the relationships of bond length-strain in the skeleton of relatively weak IV-7 under axial extension at different temperatures. Clearly, the bond length in IV-7 CNNT changes with increasing strain. At low temperatures (1-300 K), strong nonlinearity in the bond length-strain curves is identified, explaining its nonlinear elasticity as illustrated in Figure 8c. Moreover, there is a critical strain after which change in bond length becomes more pronounced as the strain is further applied. The critical strain corresponds to the slightly mechanical softening of IV-7 CNNT in Figure 8c. At high temperatures, however, the bond is almost linearly lengthened with increasing axial strain. Moreover, elongation in bond length becomes less significant with increasing axial strain. As the axial is applied to a critical value, bond length jumps because of tension induced dissociation of the bond. Figure S16 plots the variation in the bond length with global strain for mechanically robust Tube (3,0)_1245 CNNT at different temperatures. Similarly, covalent bond in the skeleton is strongly nonlinearly elongated with increasing axial strain at low temperatures. However, there are two critical strains in critical changes of bond length; Increase in the bond length becomes more pronounced as the elongation is overstrain of around 0.075, but then becomes less significant when the applied strain is over about 0.12. Such “S”-shaped curve of bond length-strain is able to explain the unique mechanical loading curve of Tube (3,0)_1245 CNNT where an initial softening but then a stiffening appears. At high temperature, the bond length is almost linearly increased with increasing axial strain, and the elongation in bond length becomes less pronounced as the axial strain is increased. Furthermore, it is observed that, at low temperatures, the bond dissociates once the bond length is over around 1.8 Å, whereas, at high temperatures, the bond is broken as the bond length below 1.8 Å. With regard to other CNNTs, it is similarly found that the bond length nonlinearly increases with increasing strain at low temperatures, whereas at high temperatures the localized bond is linearly elongated as the global axial strain is applied, as shown in Figure S17-S21.

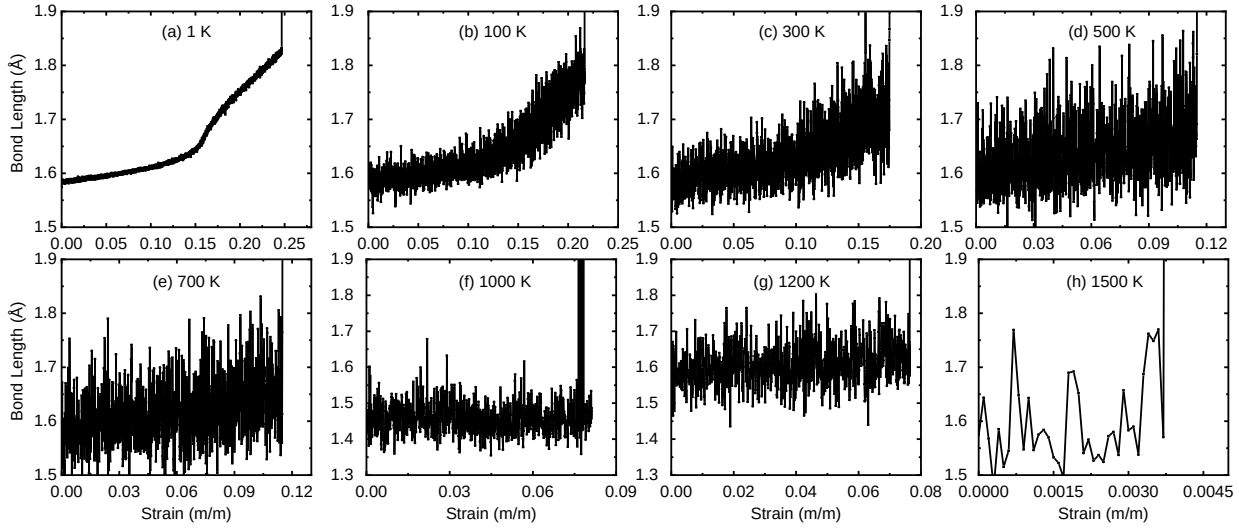

Figure S15 Development of bond length of the skeleton under tension. (a)-(h) Variation in a localized bond length with globally axial strain for IV-7 at temperature ranging from 1-1500 K.

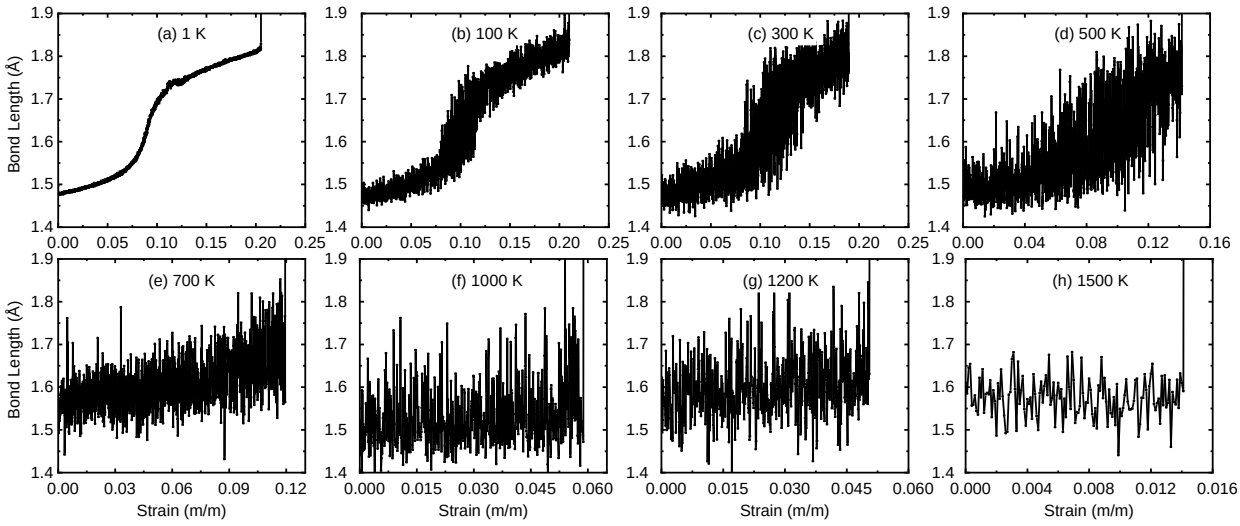

Figure S16 Development of bond length of the skeleton subjected to elongation. (a)-(h) Variation in a localized bond length with globally axial strain for Tube (3,0)_1245 CNNT at temperature from 1-1500 K.

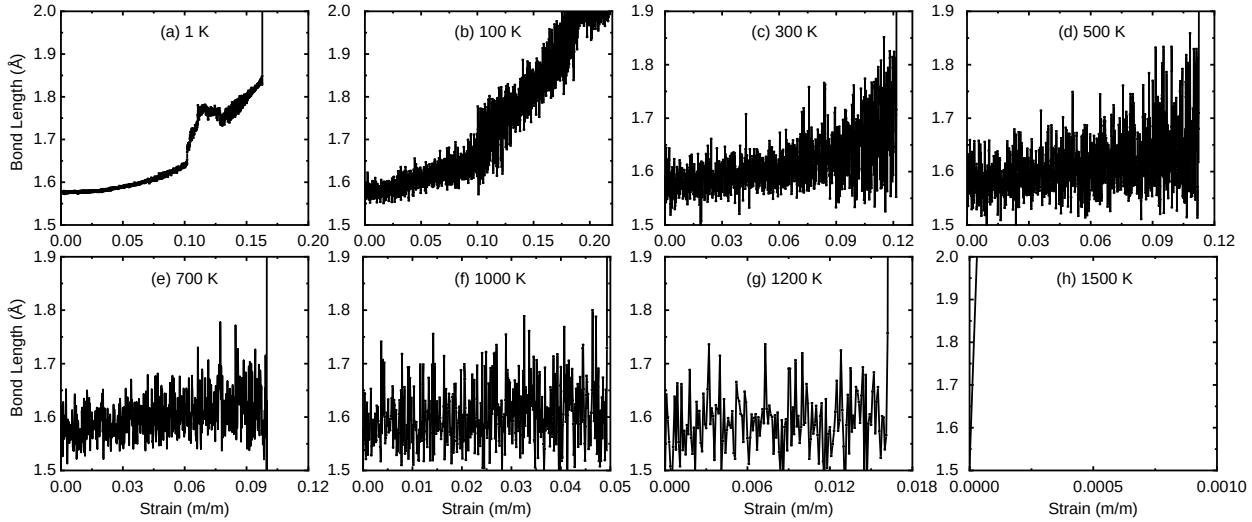

Figure S17 (a)-(h) Variation in a localized bond length with globally axial strain for Polymer I_3-3_25 at temperature from 1-1500 K, respectively.

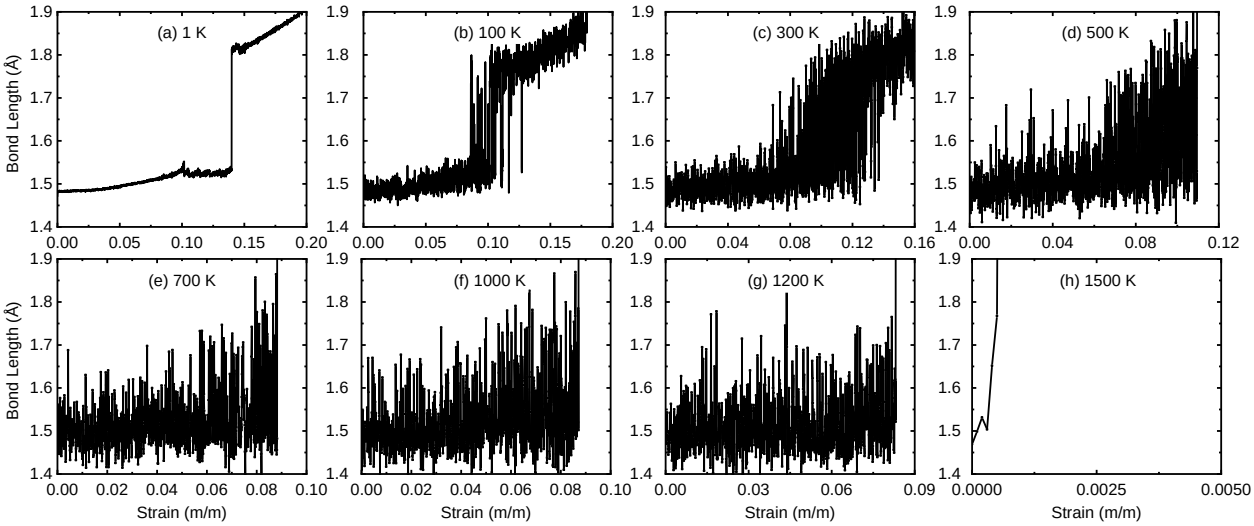

Figure S18 (a)-(h) Variation in a localized bond length with globally axial strain for Polymer I_4-2_36 at temperature from 1-1500 K, respectively.

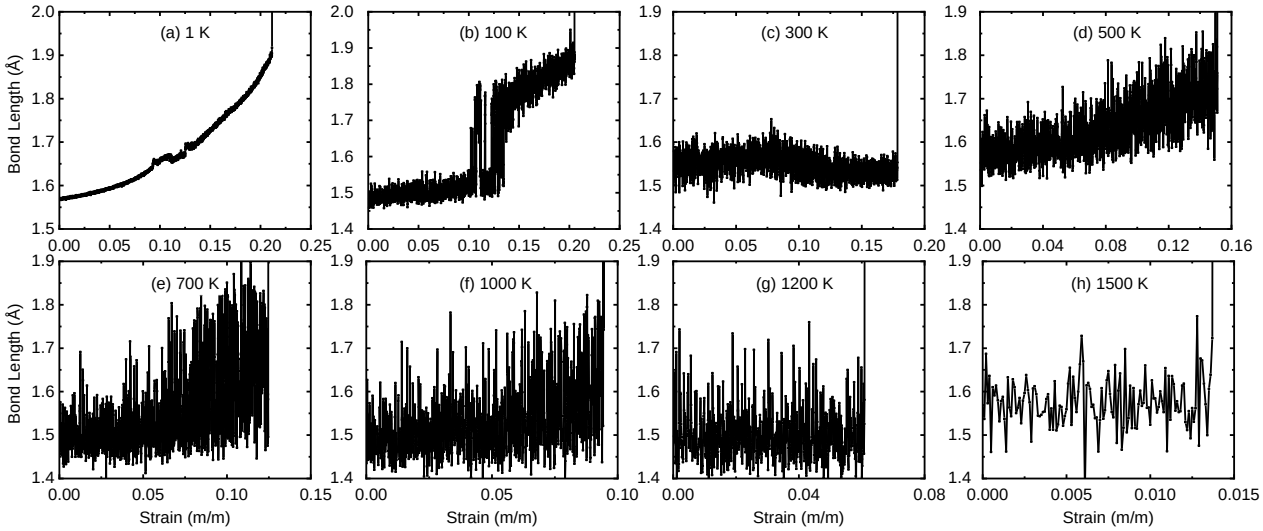

Figure S19 (a)-(h) Variation in a localized bond length with globally axial strain for Polytwistane_153 at temperature from 1-1500 K, respectively.

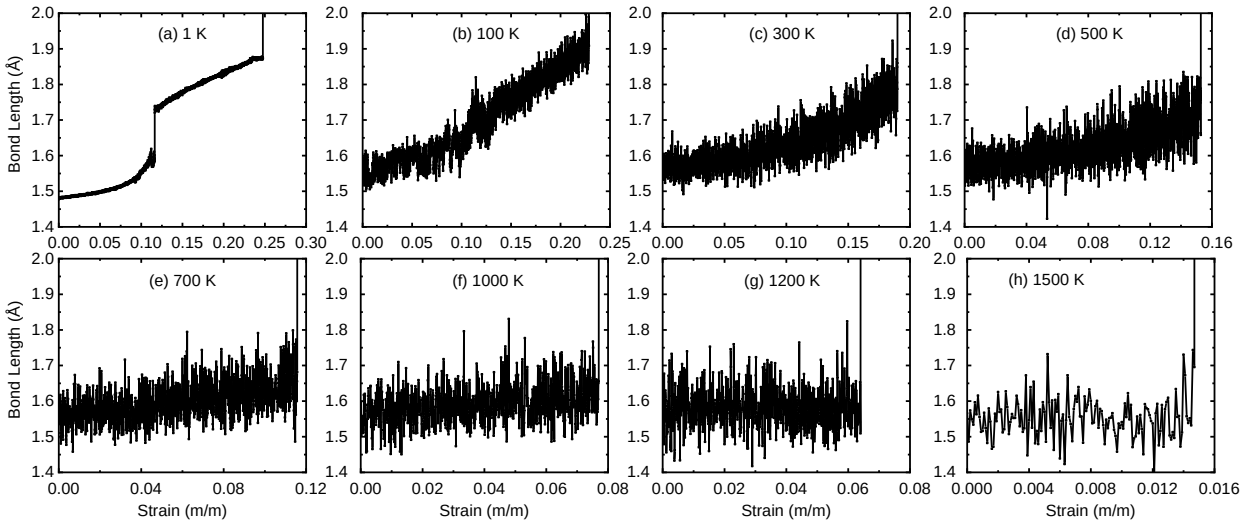

Figure S20 (a)-(h) Variation in a localized bond length with globally axial strain for Tube (3,0)_123456 at temperature from 1-1500 K, respectively.

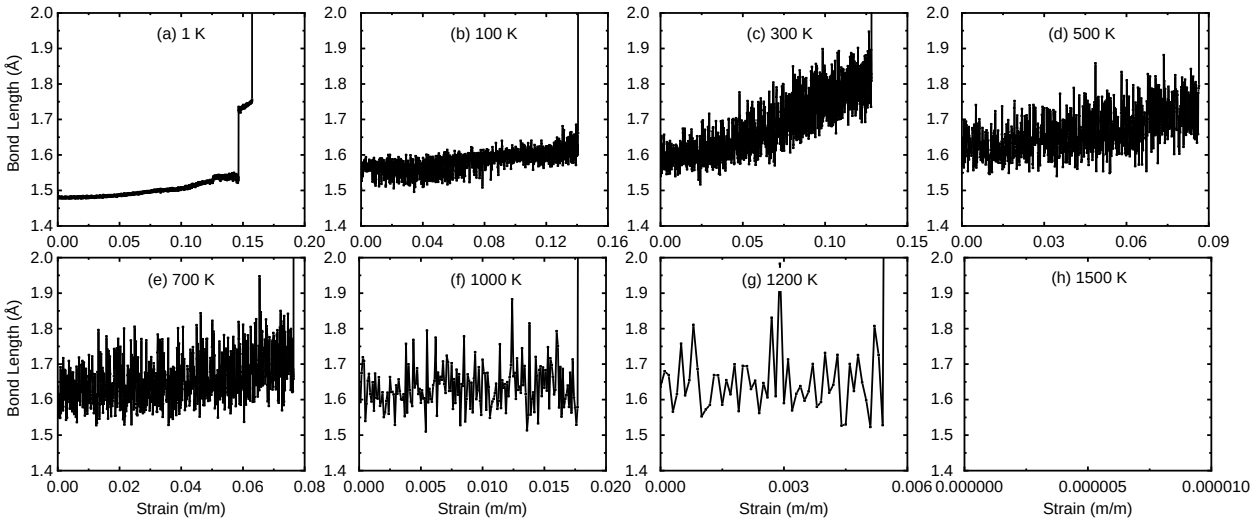

Figure S21 (a)-(h) Variation in a localized bond length with globally axial strain for Zipper polymer_24 at temperature from 1-1500 K, respectively.

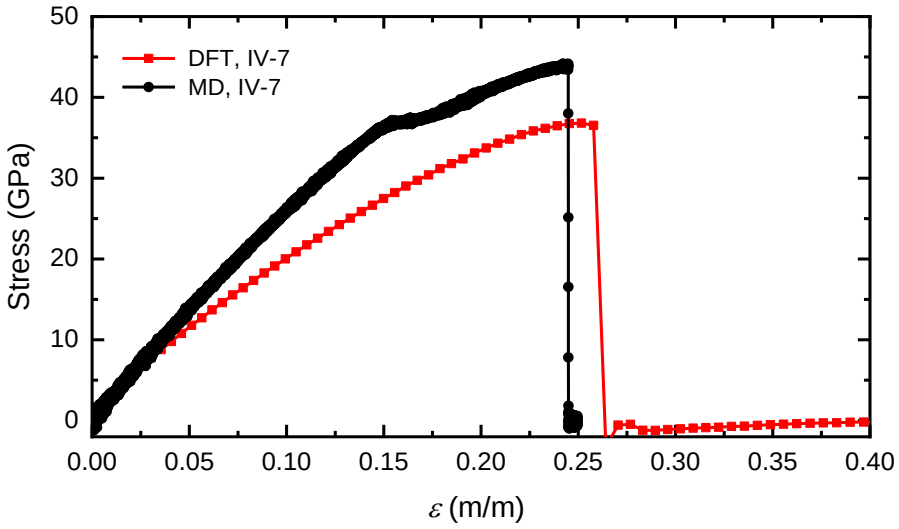

Figure S22 Comparison of global tensile stress-strain curves of selected IV-7 CNNT by DFT and ReaxFF-based MD calculations.

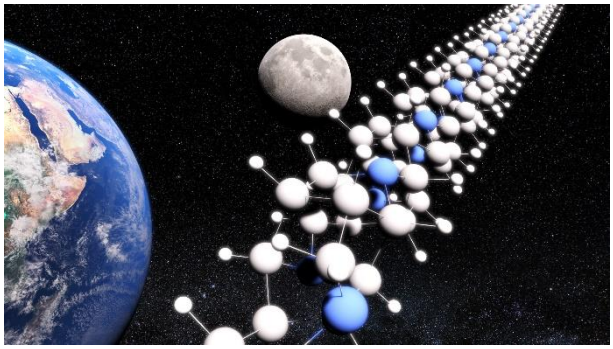

The prediction of application and mechanical properties of carbon nitride nanothreads.